

Technical Design Report on the E80 Experiment: Systematic investigation of the light kaonic nuclei

ver. June 3, 2022

H. Asano K. Itahashi, M. Iwasaki, Y. Ma, R. Murayama, H. Outa, F. Sakuma*,
T. Yamaga

RIKEN Cluster for Pioneering Research, RIKEN, Saitama, 351-0198, Japan

K. Inoue, S. Kawasaki, H. Noumi, K. Shirotori
Research Center for Nuclear Physics (RCNP), Osaka University, Osaka, 567-0047, Japan

H. Ohnishi, Y. Sada, M. Tsuruta, C. Yoshida
*Research Center for Electron Photon Science (ELPH), Tohoku University, Sendai,
982-0826, Japan*

T. Hashimoto
Japan Atomic Energy Agency (JAEA), Ibaraki 319-1195, Japan

M. Iio, S. Ishimoto, K. Ozawa, S. Suzuki
High Energy Accelerator Research Organization (KEK), Ibaraki, 305-0801, Japan

T. Akaishi
Department of Physics, Osaka University, Osaka, 560-0043, Japan

T. Nagae
Department of Physics, Kyoto University, Kyoto, 606-8502, Japan

H. Fujioka
Department of Physics, Tokyo Institute of Technology, Tokyo, 152-8551, Japan

M. Bazzi, A. Clozza, C. Curceanu, C. Guaraldo, M. Iliescu, M. Miliucci, A. Scordo,
D. Sirghi, F. Sirghi
Laboratori Nazionali di Frascati dell' INFN, I-00044 Frascati, Italy

P. Buehler, E. Widmann, J. Zmeskal
Stefan-Meyer-Institut für subatomare Physik, A-1090 Vienna, Austria

*Spokesperson, E-mail: sakuma@ribf.riken.jp

Abstract

We report on the technical design for the E80 experiment in this document. The E80 experiment aims to precisely measure kaon-nuclear bound systems (kaonic nuclei), focusing on the $\bar{K}NNN$ ($A = 3$) system as a first step toward the comprehensive study of the light kaonic nuclei from the “ $\bar{K}N$ ” ($=\Lambda(1405)$) to “ $\bar{K}NNNN$.” Through the experiments, we will provide the feature of the kaonic nuclei from the property changes depending on the mass number A , *i.e.*, nuclear density, which is related to spontaneous and explicit chiral symmetry breaking in QCD. To achieve the systematic measurements, we are now constructing a new 4π cylindrical detector system (CDS) to drastically enlarge the acceptance by detecting or identifying all the particles, including neutral particles, in the final states. We have also proposed to improve the K1.8BR beam line spectrometer by shortening the beam line to utilize $\sim 40\%$ more K^- than the current configuration.

Contents

1	Introduction	3
2	J-PARC E80 Experiment	6
2.1	Experimental Method	6
2.2	Apparatus	7
2.3	Expected Yield	8
2.4	Construction Schedule and Cost	10
3	K1.8BR Beam Line	12
4	Beam Line Spectrometer	15
4.1	Trigger Counters	16
4.2	Kaon Identification Counter	17
4.3	Beam Line Chambers	18
5	Cryogenic Target System	19
6	Cylindrical Detector System (CDS)	20
6.1	Superconducting Solenoid Magnet	22
6.2	Cylindrical Drift Chamber (CDC)	34
6.3	Cylindrical Neutron Counter (CNC)	37
6.4	Vertex Fiber Tracker (VFT)	39
6.5	Support Structure of the CDS	40
7	Trigger and DAQ systems	42
8	Acknowledgments	43

1 Introduction

The study of the $\bar{K}N$ interaction is one of the most important subjects to understand meson-baryon interactions in low energy quantum chromodynamics (QCD). Extensive measurements of anti-kaonic hydrogen atom [1–3] and low-energy $\bar{K}N$ scattering [4] have revealed the strongly attractive nature of the $\bar{K}N$ interaction in the isospin $I = 0$ channel. Consequently, the possible existence of deeply-bound kaonic nuclear states (kaonic nuclei) has been widely discussed [5–24]. Kaonic nuclei are predicted to be compact due to the strong $\bar{K}N$ attraction, suggesting that high-density nuclear matter is realized in kaonic systems.

Among the kaonic nuclei, the $\bar{K}NN$ system with $I = 1/2$ and $J^P = 0^-$ (symbolically denoted as K^-pp for the $I_z = +1/2$ state) is of special interest because it is the lightest $S = -1$ \bar{K} nucleus and whose existence is supported by many theoretical works today. Despite considerable experimental efforts over the past 20 years, it has been challenging to prove the existence of K^-pp . Several groups have reported observations of a K^-pp candidate with a binding energy of around 100 MeV in experiments measuring non-mesonic decay branches of Λp and/or $\Sigma^0 p$ in different reactions [25–27]. There are also contradicting reports concluding that the reactions can be understood without a bound state [28–31].

Recently, we confirmed the existence of the K^-pp bound state by using the simplest reaction of in-flight ${}^3\text{He}(K^-, N)$ at the J-PARC E15 experiment [32–35]. A distinct peak structure was observed well below the mass threshold of $K^- + p + p$ in the Λp invariant-mass (IM) spectrum, obtained from the ${}^3\text{He}(K^-, \Lambda p)n$ measurement as shown in Fig. 1. The simplest and most natural interpretation of this peak is K^-pp .

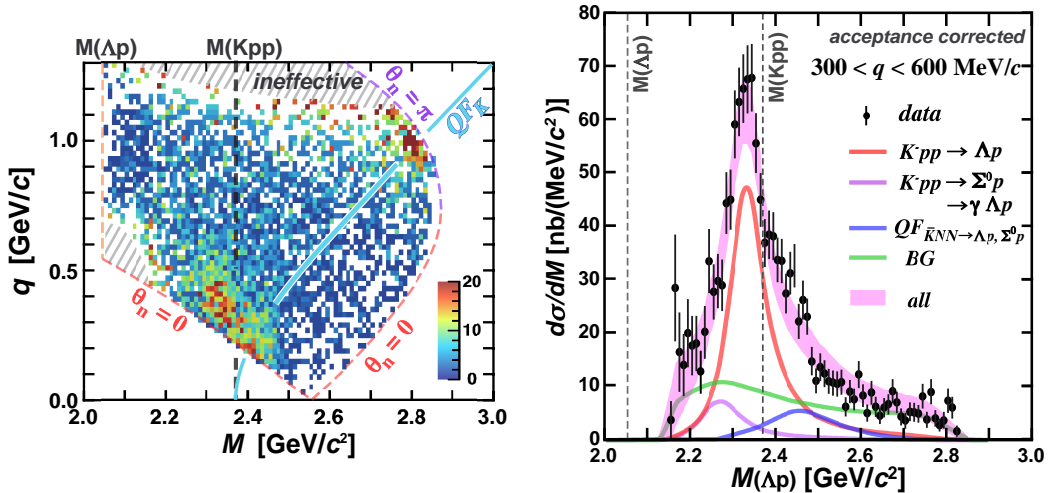


Figure 1: (left) Efficiency and acceptance corrected data over M (Λp invariant mass) and q (momentum transfer) obtained at the J-PARC E15 experiment [34, 35]. (right) Λp invariant mass in the region $0.3 < q < 0.6$ MeV/ c .

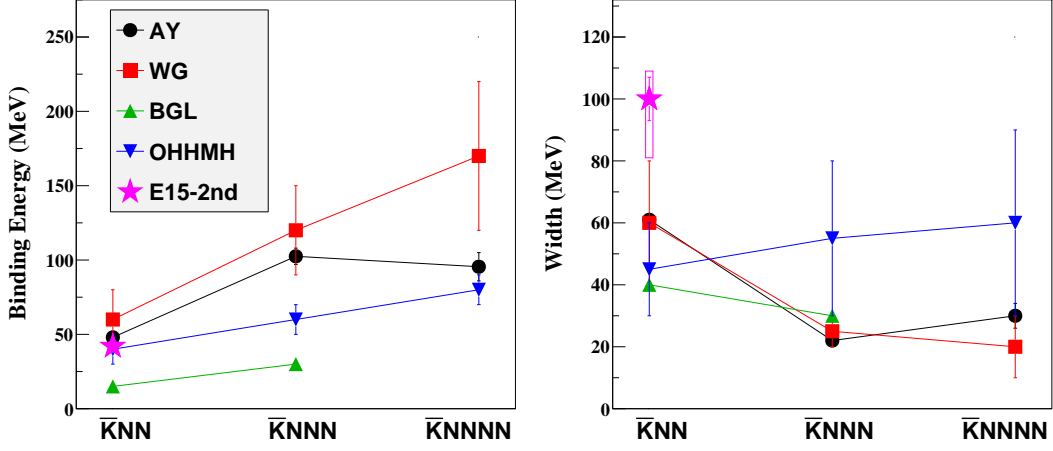


Figure 2: Summary of theoretical calculations of the kaonic nuclei from $A = 2$ to 4 in different models AY [6, 7], WG [13], BGL [16], and OHHMH [22]. The result obtained at the E15 experiment is also plotted [35].

The result obtained in the E15 experiment is experimentally solid compared to the other experiments in that we measured a wide momentum-transfer range with high statistics, however, the detailed properties need to be clarified by further experimental studies. For this purpose, we have planned a series of experimental programs using the $(K^-, N/d)$ reactions on light nuclear targets at the K1.8BR beam line. The programs will enable a detailed and systematic study of a range of nuclei from $\bar{K}N$ ($\Lambda(1405)$) to $\bar{K}NNNN$ using the world's highest intensity low-momentum kaon beam at J-PARC. The programs comprise:

- [$\bar{K}N(\Lambda(1405))$] Precise measurement of the $\Lambda(1405)$ state in large momentum transfer region via the $d(K^-, n)$ reaction, to experimentally clarify the picture whether it is a baryonic state or a $\bar{K}N$ molecular state,
- [$\bar{K}NN$] Investigation of the spin and parity of the $\bar{K}NN$ state via the ${}^3\text{He}(K^-, N)$ reactions,
- [$\bar{K}NNN$] Precise measurement of the $\bar{K}NNN$ states via the ${}^4\text{He}(K^-, N)$ reactions, as for the bridge to access heavier system, and,
- [$\bar{K}NNNN$] Advanced search for the $\bar{K}NNNN$ states via the ${}^6\text{Li}(K^-, d)$ reaction.

In the series of experimental programs, we aim to determine the mass number dependence of the binding energy, decay width, and system size beyond $\bar{K}NN$. The mass number dependence has been calculated with several theoretical models, as summarized in Fig. 2. The calculated values of the binding energy and decay width vary

widely due to the differences in the $\bar{K}N$ interaction models, however, almost all the calculations show that the larger nuclei have stronger binding energies. As for the width, there does not appear to be as large mass number dependence as the binding energy, in which the calculations take into account only mesonic decay channels, such as $\pi\Sigma N$ and $\pi\Lambda N$. The calculated width is expected to be larger if the models adopt non-mesonic decay channels, as demonstrated in Ref. [17].

In parallel to these studies, we also intend to access the $S = -2$ kaonic nuclei, such as the theoretically predicted K^-K^-pp state. The $S = -2$ system could allow us to access even higher density systems than the $S = -1$ kaonic nuclei. As described in our Letter of Intent [36], one possible approach for the measurements at J-PARC could be:

- [$\bar{K}\bar{K}NN$] Searching for $\bar{K}\bar{K}NN$ states via $\bar{p}^3\text{He}$ annihilation.

To ensure the measurements are systematic and precise, we are constructing a new 4π spectrometer to measure all the particles involved in the reactions and to reconstruct the formation and decay of the kaonic nuclei exclusively. The spectrometer is designed to be highly versatile so that all the experiments can be performed simply by changing the target materials. In addition, for more efficient use of the high-intensity kaon beam, we have proposed shortening the existing K1.8BR beam line for a larger kaon yield without deteriorating the momentum resolution of the kaon beam.

In this document, we describe technical details about the new spectrometer to conduct an experimental study of the $\bar{K}NNN$ bound state for the first step, toward the systematic investigation of the light kaonic nuclei.

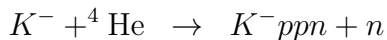
2 J-PARC E80 Experiment

We aim to measure the $\bar{K}NNN$ ($A = 3$) system at the E80 experiment, as the first step toward a comprehensive study. E80 will provide the mass number dependence of the kaonic nuclei for the first time. The dependence can more clearly reveal the $\bar{K}N$ interaction below the mass threshold, by comparing the obtained properties of the $\bar{K}NNN$ state with those of the already reported K^-p ($\Lambda(1405)$) and K^-pp states.

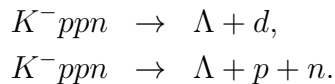
2.1 Experimental Method

The key to the experimental search is to adopt a simple reaction and to measure it exclusively. The adoption of a simple reaction, such as in-flight \bar{K} induced reactions with light target nuclei, enables us to specify the reaction channel by minimizing the contribution of reactions unrelated to the kaonic nuclei formation. Exclusive measurements are crucial for distinguishing small and broad signals from the large and widely distributed quasi-free and multi-nucleon absorption backgrounds. From the experience of E15, we have learned that reducing the number of particles in the final state is a key to removing ambiguity in interpreting the reaction process; more specifically, pion contribution such as from quasi-free Y^* production complicates interpreting reactions. Therefore, we focus on the $K^-ppn \rightarrow \Lambda d$ and Λpn decay channels in ${}^4\text{He}(K^-, \Lambda d/\Lambda pn)n$ reactions.

In the E80 experiment, we will perform exclusive measurements of the production and decay of the K^-ppn state using the in-flight reaction



followed by the expected non-mesonic decays



To maximize the (\bar{K}, N) reaction rate at around zero degrees as shown in Fig 3, we will utilize 1.0 GeV/ c incident kaons. We will determine the binding energy and width from the invariant mass reconstruction of the decays. The invariant mass needs to be obtained in the wide momentum transfer region to distinguish the bound-state production from the quasi-free processes by the event kinematics as demonstrated in the E15 analysis.

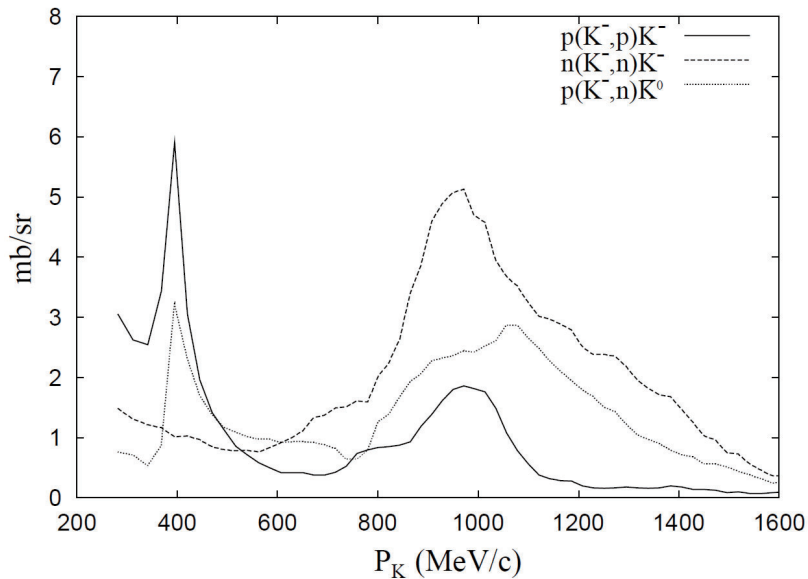


Figure 3: Cross sections of the $K^-N \rightarrow \bar{K}N'$ reactions at $\theta_n = 0^\circ$ (nucleon forward / kaon backward) [37].

2.2 Apparatus

The incoming K^- beam will be identified and its momentum will be analyzed by the beam-line spectrometer. The beam kaon will be incident on a liquid ^4He target located at the final focus point, and particles generated from the reactions will be measured with a cylindrical detector system (CDS) surrounding the target system. A forward or backward going particle out of the CDS acceptances will be identified using missing mass technique, thus all the particles from the reactions will be identified. A design of the CDS is shown in Fig. 4. It is mainly composed of a large superconducting solenoid magnet, a cylindrical wire drift chamber (CDC), and a cylindrical neutron counter (CNC). The details of each apparatus used for the experiment are described from Sec. 4.

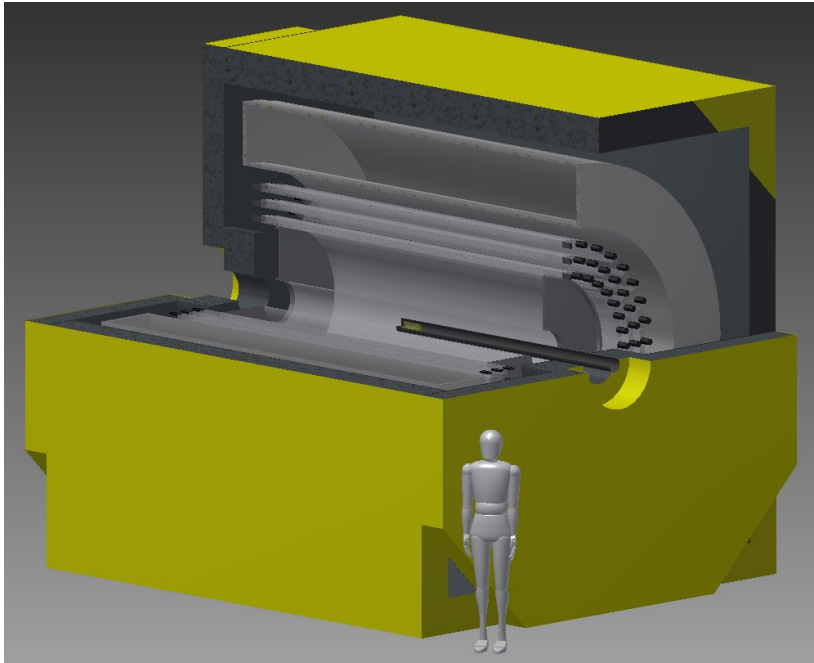


Figure 4: Design of the CDS.

2.3 Expected Yield

Recently, we have conducted a prompt analysis on Λdn final state of $K^-^4\text{He}$ reaction at 1 GeV/c using the T77 data, and found a kinematical anomaly below the mass threshold of $M(K^-ppn)$ having quite similar structure to that of Λpn final state of $K^-^3\text{He}$ reaction [38]. As in the case of the $\bar{K}NN$ bound state in the Λpn final state, the observed structure in the Λdn final state would be the signal of the K^-ppn bound state. The cross section of the peak structure has been preliminary evaluated to be $\sim 5 \mu\text{b}$, which is smaller than the initial estimate in the E80 proposal. To estimate the expected yield of the K^-ppn , we use this preliminary evaluated cross section for the $K^-ppn \rightarrow \Lambda d$ decay, and we assume that the $K^-ppn \rightarrow \Lambda pn$ branching ratio is the same as the Λd decay, *i.e.*,

$$\begin{aligned}\sigma_{Kppn}^{tot} \cdot BR(\Lambda d) &\sim 5 \mu\text{b}, \\ \sigma_{Kppn}^{tot} \cdot BR(\Lambda pn) &\sim 5 \mu\text{b}.\end{aligned}$$

The detector acceptance of the CDS (Ω_{CDS}) is evaluated with a full detector simulation using the GEANT4 toolkit ver.10.2.3 with the “QGSP_BERT_HP” physics list [39].

The estimated yields for each channel normalized by 1 G (10^9) K^- beam at trigger level are summarized in Table 1. The CDS acceptance of Ω_{CDS} is obtained for the exclusive reconstruction of $^4\text{He}(K^-, \Lambda d/\Lambda pn)n$. The yields are calculated using the

following equation:

$$\begin{aligned}
 N &= \sigma \times N_{beam} \times N_{target} \times \epsilon, \\
 \epsilon &= \epsilon_{DAQ} \times \epsilon_{trigger} \times \epsilon_{beam} \times \epsilon_{fiducial} \times \Omega_{CDS} \times \epsilon_{CDS},
 \end{aligned}$$

where

- N : expected yield,
- σ : cross section including the decay branching ratio,
- N_{beam} : number of the beam kaons,
- N_{target} : number of the target particles,
- ϵ : total experimental efficiency,
- ϵ_{DAQ} : DAQ efficiency,
- $\epsilon_{trigger}$: trigger efficiency,
- ϵ_{beam} : analysis efficiency of the beam kaons,
- $\epsilon_{fiducial}$: efficiency of fiducial volume selection,
- Ω_{CDS} : detector acceptance of the CDS,
- ϵ_{CDS} : analysis efficiency of the CDS.

In the calculation of N_{target} , fiducial volume length of 11.8 cm is adopted, which was set to the T77 analysis. Ω_{CDS} for the Λpn channel is evaluated with 15 cm thick plastic scintillation counter as the CNC, in which the neutron detection efficiency is obtained to be ranging from $\sim 15\%$ (at ~ 0.2 GeV/ c) to $\sim 3\%$ (at ~ 1.0 GeV/ c) from the Geant4 simulation. We assume the same parameters obtained and evaluated in the analysis of the predecessor experiments at the K1.8BR: $\epsilon_{DAQ} = 0.92$, $\epsilon_{trigger} = 0.98$, $\epsilon_{beam} = 0.72$, and $\epsilon_{fiducial} = 0.65$. The analysis efficiencies of the CDS, $\epsilon_{CDS} = 0.6$ for Λd channel and $\epsilon_{CDS} = 0.3$ for Λpn channel, are assumed based on the result of $K^{-3}\text{He} \rightarrow \Lambda pn$ analysis and the preliminary result of $K^{-3}\text{He} \rightarrow \pi \Sigma pn$ analysis, respectively.

At the improved K1.8BR beam line, we expect 2.7×10^5 kaons on target per spill with the momentum of 1.0 GeV/ c , under the MR beam power of 90 kW. Table 2 shows the estimated yields with 3 weeks beam time under assumption of 90% accelerator up-time: 100 G kaons on target (155 G beam kaon at kaon-trigger level without fiducial volume selection).

Table 1: Estimated yield of the K^-ppn bound state normalized by 1 G (10^9) K^- beam at trigger level.

decay mode	Λd	Λpn
$\sigma^{tot} \cdot BR$	assumed to be $5 \mu\text{b}$	
N_{beam}	10^9	
N_{target}	2.56×10^{23}	
ϵ_{DAQ}	0.92	
$\epsilon_{trigger}$	0.98	
ϵ_{beam}	0.72	
$\epsilon_{fiducial}$	0.65	
Ω_{CDS}	0.23	0.059
ϵ_{CDS}	0.6	0.3
N	80	10

Table 2: Estimated K^-ppn yield for three-week data taking under the MR beam power of 90 kW.

decay mode	Λd	Λpn
$\sigma^{tot} \cdot BR$	assumed to be $5 \mu\text{b}$	
accelerator up-time	0.9	
# of K^- beam	155×10^9	
# of K^- on target	100×10^9	
# of expected yield	1.2×10^4	1.5×10^3

2.4 Construction Schedule and Cost

The construction of the E80 experimental setup has been started from FY2022 with research grants "Grant-In-Aid for Specially Promoted Research by MEXT (FY2022-26)". The main detector components of the cylindrical detector system (CDS) for E80, *i.e.*, the superconducting solenoid magnet, the cylindrical drift-wire chamber (CDC), and the first layer of the cylindrical neutron counter (CNC), will be covered within the current budget situation. The rest of the CNC will be built with budgets from other sources that we are currently trying to acquire. A vertex fiber tracker will be ready in FY2022 for the E73 experiment. A liquid $\text{H}_2/\text{D}_2/{}^3,4\text{He}$ target system, which has been worked well at the K1.8BR, will also be prepared for the E80 setup with minor modification.

The schedule for the E80 preparation is shown in Fig. 5. The spectrometer design,

	FY2022				FY2023				FY2024				FY2025				2026~	
	Q1	Q2	Q3	Q4	Q1	Q2	Q3	Q4	Q1	Q2	Q3	Q4	Q1	Q2	Q3	Q4		
SC Solenoid	Design	Purchase (SC Wire)		Construction				Installation	Test	Integration	Commissioning	Physics Run	Analysis & Publication					
NC	Design	Purchase (Scinti.)		Construction				Test & Commissioning										
CDC	Design			Modification				Test & Commissioning										
K1.8BR Beam Line			E73 Experiment					Upgrade					E80 Experiment					

Figure 5: Schedule of the preparation for the E80 experiment.

including the magnet and detector support structure therein, will be completed in the first half of FY2022. Then we will start the construction of the first layer of the CNC, which will be completed in FY2023. The CDC will be constructed in FY2023, and commissioning will start in the beginning of FY2024. The superconducting solenoid magnet will be completed by the end of FY2024, following excitation testing and magnetic field measurement. Thus, the installation of the magnet at the K1.8BR beam line will be conducted around the end of FY2024, and integration of the cylindrical detector system will be completed in the first half of FY2025.

We are now working on a realistic design of the K1.8BR area configuration with shielding calculation using MARS code, in close cooperation with the HD-BL group. Cost estimation has also been started. We expect the beam-line modification will be conducted around FY2024 with a facility budget.

The E80 experiment thus will be ready for the experiment at the K1.8BR beam line in FY2025. We expect the Phase-II approval will lead to follow-up funding and foster collaborations, in particular, young Ph.D students and full-time postdoctoral fellows.

3 K1.8BR Beam Line

The E80 experiment will be conducted at the K1.8BR beam line. To achieve efficient utilization of the K^- beam at E80, we have proposed a new configuration of the beam line as shown in Fig. 6. By this new setup, the available number of kaons on target are expected to increase by ~ 1.4 times compared to the present beam line configuration without deteriorating the momentum resolution of the kaon beam.

In the improvement, we have proposed removing the D5 magnet so that the available kaon yield is maximized. Since the beam trajectory is drastically changed by the removal, the beam dump is also required to be moved along the beam direction. Therefore, we have requested to rearrange the K1.8BR experimental area as shown in Fig. 6. At the modified experimental area, the beam dump is moved from the west side of the hadron hall currently installed to the north side. The experimental area must be large enough to install the large CDS along the beam axis.

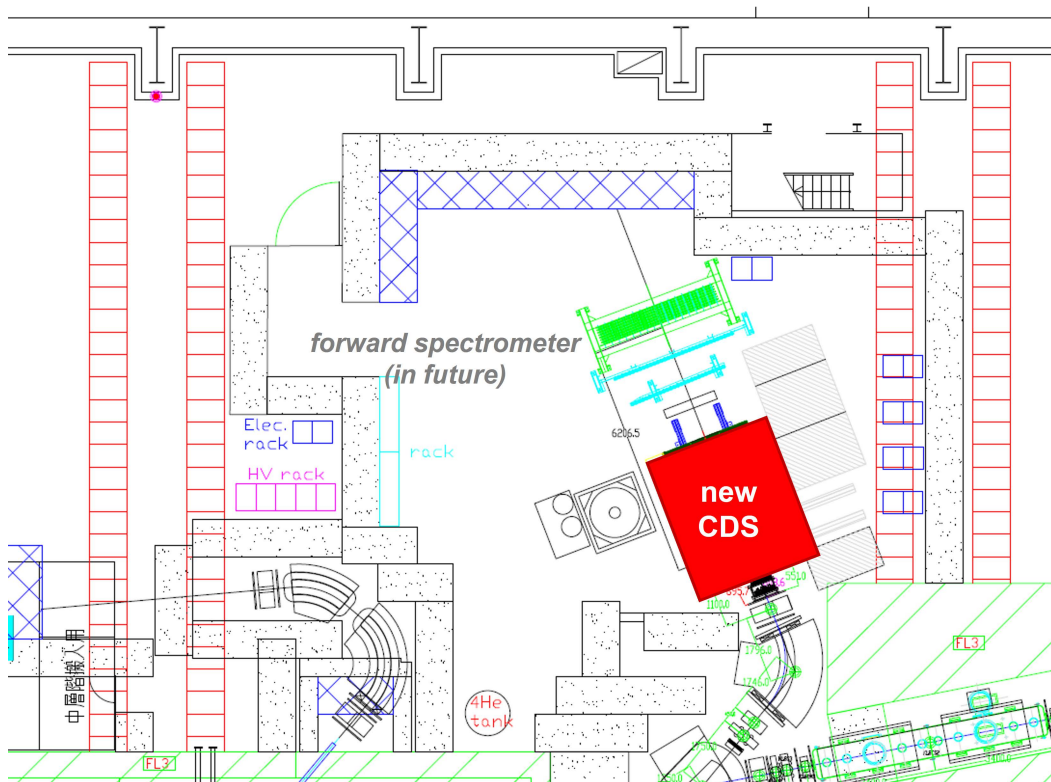


Figure 6: Plan of a layout of the K1.8BR experimental area for the proposed experiment.

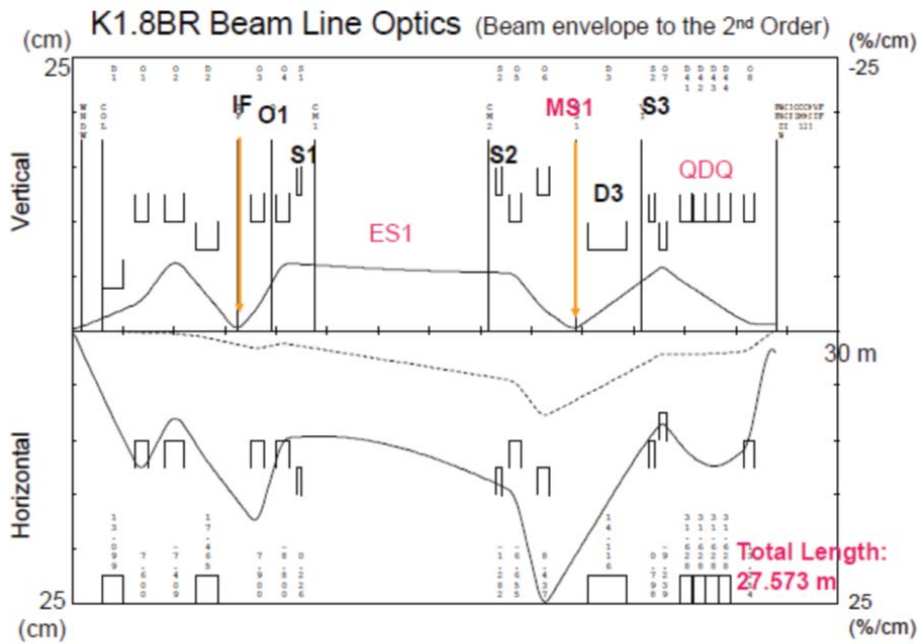


図8 : K1.8BR ビームエンベロープ

Figure 7: Beam-line optics of the improved K1.8BR beam line.

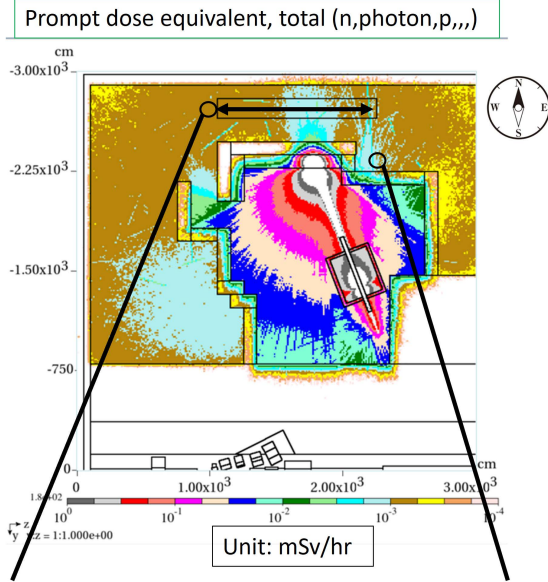
The evaluated beam optics with the new beam-line setup is shown in Fig. 7. With this modification, the beam-line length will be shortened by ~ 2.5 m[†]. The beam focus is evaluated to be at least the same size as the current beam line configuration. Thus, the available kaons on target are conservatively estimated to increase ~ 1.4 times, which corresponds to 2.7×10^5 kaons on target per spill at the beam power of 90 kW with 4.2 s repetition cycle[‡].

Figure 8 shows the calculated results of radiation level using MARS code with realistic K1.8BR design. In the calculation, 5.0×10^6 pions per second (corresponding to the current operational limit of 1.8×10^{10} pions per hour at the K1.8BR) are exposed from the center of the D4 magnet to the beam dump with pencil-beam size. The results include the safety factor of four, namely, the calculation results are multiplied by four. At all points outside of the experimental area, the radiation level is below the limit of $25 \mu\text{Sv/h}$.

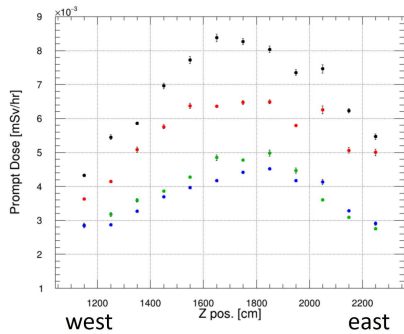
[†]In the original beam-line design, the beam-line length will be shortened by ~ 3.7 m with the removal of D5, but the final focusing point will be shifted to the downstream of the beam line by ~ 1.2 m because the size of the new CDS becomes larger than the currently used CDS as described in Sec. 6.

[‡] 2.6×10^5 (Run87, 2021 @ 64 kW, 5.2 s) $\times 0.65$ (fiducial volume selection) $\times 1.4$ (beam line length) $\times 90 / (64 * 5.2 / 4.2)$ (beam power) $\sim 2.7 \times 10^5$ (@ 90 kW, 4.2 s).

At the beam height :150~250 cm sliced



**Catwalk position,
east-west dependence**



**Stair position,
up-down dependence**

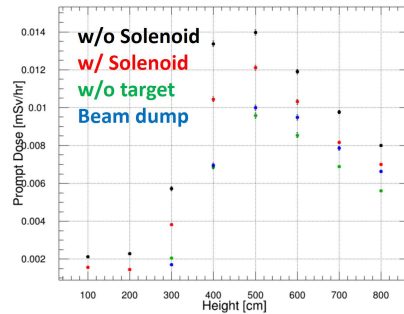


Figure 8: Shielding calculation of the modified K1.8BR area using MARS code. Results are shown in case that 5.0×10^6 pions per second (corresponding to the current operational limit of 1.8×10^{10} pions per hour at the K1.8BR) are exposed from the center of the D4 magnet to the beam dump with pencil-beam size. Iron (Fe) target of 2 cm thickness is used for an experimental target located at the final focus point as the most severe estimation. The results include the safety factor of four, namely, the calculation results are multiplied by four. The calculated result of the radiation level at the beam height (150-250 cm sliced) is shown as a color map. The east-west dependence of the radiation level at the catwalk position (650-750 cm height) and the up-down dependence at the stair position are also shown as the left and right plots, respectively. In the plots, the calculated results with and without the solenoid magnet (red and black points), without the Fe target (green), and the result when the beam is exposed just before the beam dump (blue) are shown, respectively. At all points outside of the experimental area, the radiation level is below the limit of $25 \mu\text{Sv/h}$.

4 Beam Line Spectrometer

A schematic view of the beam line spectrometer is presented in Fig. 9. It is composed of beam line magnets, trigger counters, a beam line chamber, and a kaon identification counter.

The beam trigger is generated by a coincidence signal of a beam hodoscope tracker (BHT) and a time zero counter (T0); the flight length between the BHT and T0 is 4.0 m. The TOF resolution between the BHT and T0 is expected to be ~ 160 ps (σ), which is enough to discriminate between kaons and pions. To select the beam hitting the target in trigger level, a beam definition counter (DEF) is installed just upstream of the target. The kaon beam with momentum around 1.0 GeV/ c is identified by rejecting the pion beam using an aerogel Cherenkov counter (AC) with a refractive index of 1.05.

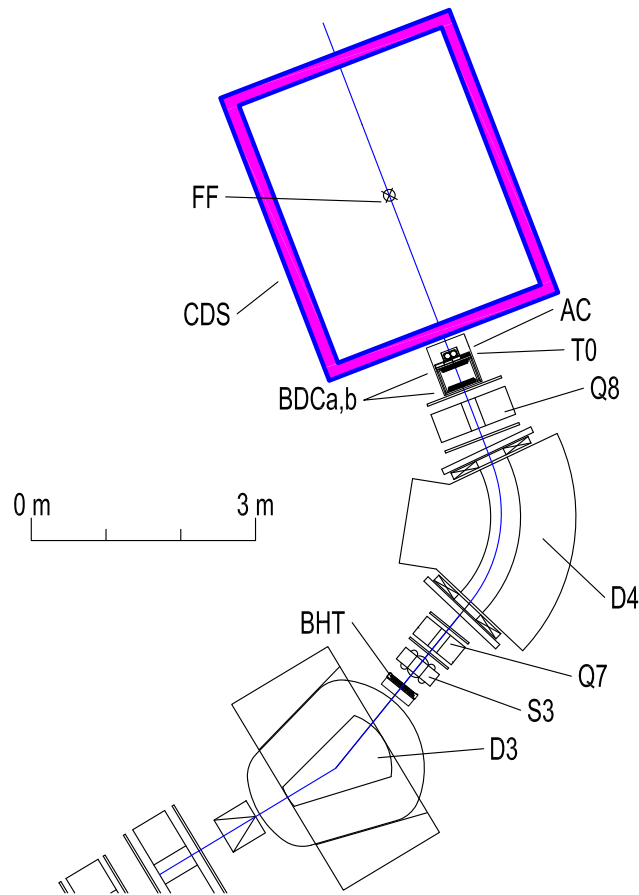


Figure 9: Schematic view of the beam line spectrometer, which consists of trigger counters (BHT and T0), a beam line chamber (BDC), and a kaon identification counter (AC).

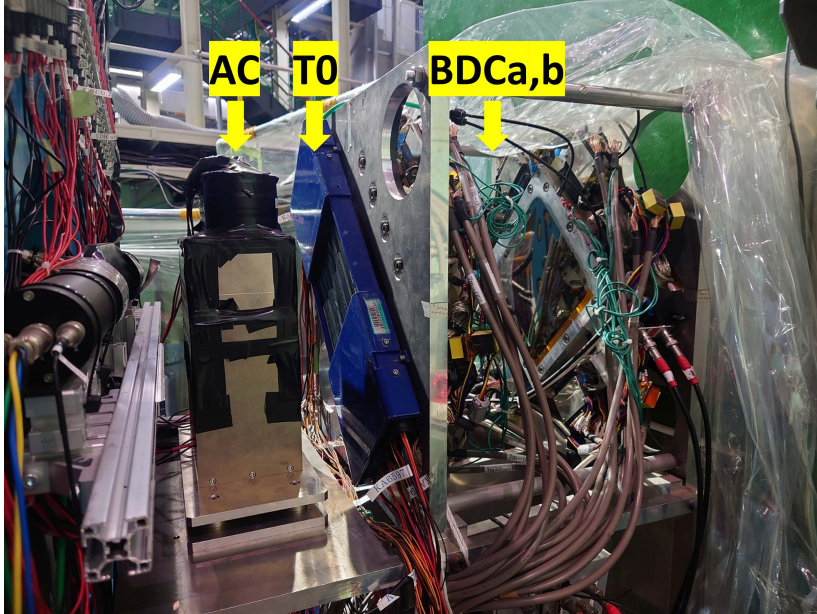


Figure 10: Current setup around the entrance of the existing solenoid magnet, and these detectors will be used as they are in the E80 setup.

The kaon beam is tracked with two beam trackers: the BHT and a beam line chamber (BDC). The momentum of the kaon is analyzed with this tracking information together with the beam optics of the D4 beam line magnet (a second-order transport matrix). The expected momentum resolution is 2×10^{-3} , which is enough for E80 as in the case of E15. To determine the reaction vertex, beam trajectory just upstream of the experimental target is also measured by a drift chamber (VDC).

All the apparatus are existing and have been well studied at the current K1.8BR beam line except for the BHT that is currently being prepared for the E73 experiment scheduled in FY2022-23. Figure 10 shows the current setup around the entrance of the existing solenoid magnet, and these detectors will be used as they are in the E80 setup.

4.1 Trigger Counters

Beam Hodoscope Tracker (BHT)

The BHT is a segmented plastic scintillation counter located downstream of the D3 magnet. Each scintillator is made of Eljen EJ-228 with a unit size of 150 mm (height) \times 7.5 mm (width) \times 3 mm (thickness). 64 segments in total are arranged in staggered two layers, each layer having 32 segments with 2.5 mm spacing in between. Therefore, effective horizontal coverage is 320 mm, and the horizontal position resolution is ~ 0.72 mm ($= 2.5/\sqrt{12}$). The scintillation light is detected by a pair of two 3×3 mm² Hamamatsu S13360-3050PE MPPCs (Multi-Pixel Photon Counter) connected in

series that are attached to the top and bottom ends and read out with AD8000-based amplifiers. The BHT is now being prepared for use in the E73 experiment scheduled to run spring 2023, aiming at replacement of the currently used and outdated beam hodoscope counter (BHD).

Time Zero Counter (T0)

T0 is a segmented plastic scintillation counter located downstream of the D4 magnet. T0 has an effective area of 160 mm (horizontal) \times 160 mm (vertical) segmented into 5 units horizontally. The unit size of the Saint-Gobain BC420 scintillator in T0 is 160 mm (height) \times 32 mm (width) \times 10 mm (thickness). To avoid over-concentration of the beam on one segment, T0 is rotated by 45 degrees in the xy plane. The scintillation light is detected by a pair of 3/4 inch Hamamatsu H6612B photomultipliers that are attached to the top and bottom ends. Since the coincidence rate of the top and bottom photomultipliers reaches ~ 1 M counts per spill, the high voltage boosters of all the photomultipliers are modified to supply adequate current to the last three dynodes.

Beam Definition Counter (DEF)

The DEF is installed just upstream of the target vacuum vessel to improve data quality and efficiency of data acquisition. Under the current and planned magnetic spectrometer setup, about 65% of the kaon beam hits the liquid target due to the large beam spot size at the final focused point. Thus the DEF is used for selecting the central region of the beam at the trigger level by adding the DEF signal to the beam trigger made by the coincidence signal of the BHT and T0.

For the DEF, a thin scintillation counter array is adopted. The DEF has an effective area of 100 mm (horizontal) \times 110 mm (vertical) segmented into 5 units horizontally, which is made of Eljen EJ-230 with a unit size of 100 mm (height) \times 20 mm (width) \times 3 mm (thickness). The scintillation light is detected by a pair of four Hamamatsu S13360-3050PE MPPCs connected in series that are attached to the top and bottom ends.

4.2 Kaon Identification Counter

For the kaon beam trigger, an aerogel Cherenkov counter (AC) located downstream of T0 is used to identify the kaon. An aerogel radiator with a refraction index of 1.05 is used as a threshold-type Cherenkov counter to reject pions in the momentum region from 0.7 GeV/ c to 1.15 GeV/ c . The AC has an effective area of 180 mm (width) \times 100 mm (height) \times 100 mm (thickness) which covers the whole distribution of the kaon beam. Cherenkov photons radiated in the beam direction are diffused in the aerogel and reflected by the thin mirror foils surrounding it, and reached at four photomultipliers on the top and bottom. Three-inch fine-mesh type photomultipliers (Hamamatsu R5543) are used to keep working with fringing fields of the Q8 magnet and the CDS magnet. A typical pion detection efficiency is more than 99%. The miss identification ratio of a kaon as a pion is about 1%.

4.3 Beam Line Chambers

Beam Line Chamber (BDC)

The BDC consists of two sets of drift chambers with the same design, BDCa and BDCb, which have 8 layers ($UU'VV'UU'VV'$ configuration). In the U and V layers the wires are tilted by ± 45 degrees. Each layer contains 32 sense wires with a drift length of 2.5 mm corresponding to an effective area of $160 \text{ mm} \times 160 \text{ mm}$. The number of readout channels is 256 for both BDCa and BDCb, which are installed ~ 300 mm apart upstream of the Q8 magnet.

The BDC uses $12.5 \mu\text{m}$ diameter gold-plated tungsten wires with 3% rhenium and $75 \mu\text{m}$ diameter copper-beryllium wires for the sense and potential wires, respectively. The cathode planes are made of $12.5 \mu\text{m}$ aluminized Kapton. The readout electronics of both chambers consist of a preamplifier card with amplifier-shaper-discriminator ICs (ASD, SONY-CXA3653Q [40], $\tau = 16$ ns) mounted on the chambers and a TDC. The output signal of the ASD board is sent to the HUL multi-hit TDC via 7m long twisted-pair cables. The chamber gas is an argon-isobutane mixture passed through a methylal (dimethoxymethane) bubbler at a refrigerator temperature of 4°C with a ratio of 76% (Ar), 20% (isobutane), and 4% (methylal). The operating voltage of the BDC is set at -1.25 kV on both the potential wires and the cathode planes. Typical position resolution of $150 \mu\text{m}$ and detection efficiency of 99% have been obtained.

Beam Vertex Chamber (VDC)

A beam vertex chamber (VDC) is installed just upstream the target cell to determine the reaction vertex point precisely. The VDC is a compact circular planar drift chamber whose size is 237 mm in diameter and 92.2 mm in height. The VDC consists of 8 layers ($XX'YY'XX'YY'$), where the wires of the Y layer are tilted by 90 degrees. Each layer contains 32 sense wires with a drift length of 3.0 mm corresponding to an effective area with a 197 mm diameter. The number of readout channels is 256. The cathode planes are made of $9 \mu\text{m}$ carbon aramid foil, and the sense and potential wires, readout electronics, and gas mixture of the VDC are the same as those for the BDC. The operational voltage of the VDC is set at -1.50 kV on both the potential wires and the cathode planes. Typical position resolution of $150 \mu\text{m}$ and detection efficiency of 99% have been obtained.

5 Cryogenic Target System

The main target nucleus for the E80 experiment is ${}^4\text{He}$. To realize a reasonable reaction rate, we use liquid ${}^4\text{He}$ as the target. We use a pulse tube refrigerator system developed for the hypertriton-lifetime measurement (J-PARC E73 experiment), which has been successfully operated at the K1.8BR beam line. The system employs a 4 K pulse tube cryocooler, the Cryomech PT410 cold head with CPA286i compressor. The system has the capability to liquefy all types of $\text{H}_2/\text{D}_2/{}^3\text{He}/{}^4\text{He}$ gasses with the same system, hence the system is designed to be explosion-proof. We will extend the horizontal part of the system to fit with the newly constructed CDS. Figure 11 shows a schematic design of the target system with the E80 setup whose detail is described in the next section. The system will be installed from downstream of the beam using rails laid on the floor, as is currently the case. In E80, a target cell composed of a Kapton cylinder and Mylar caps developed for E73 is used. The dimension is 6.8 cm in diameter and 14.2 cm in length. The achievable temperature of the system is 2.7 K, in which the density of the liquid ${}^4\text{He}$ is 0.144 g/cm^3 with a stability of better than 0.1%.

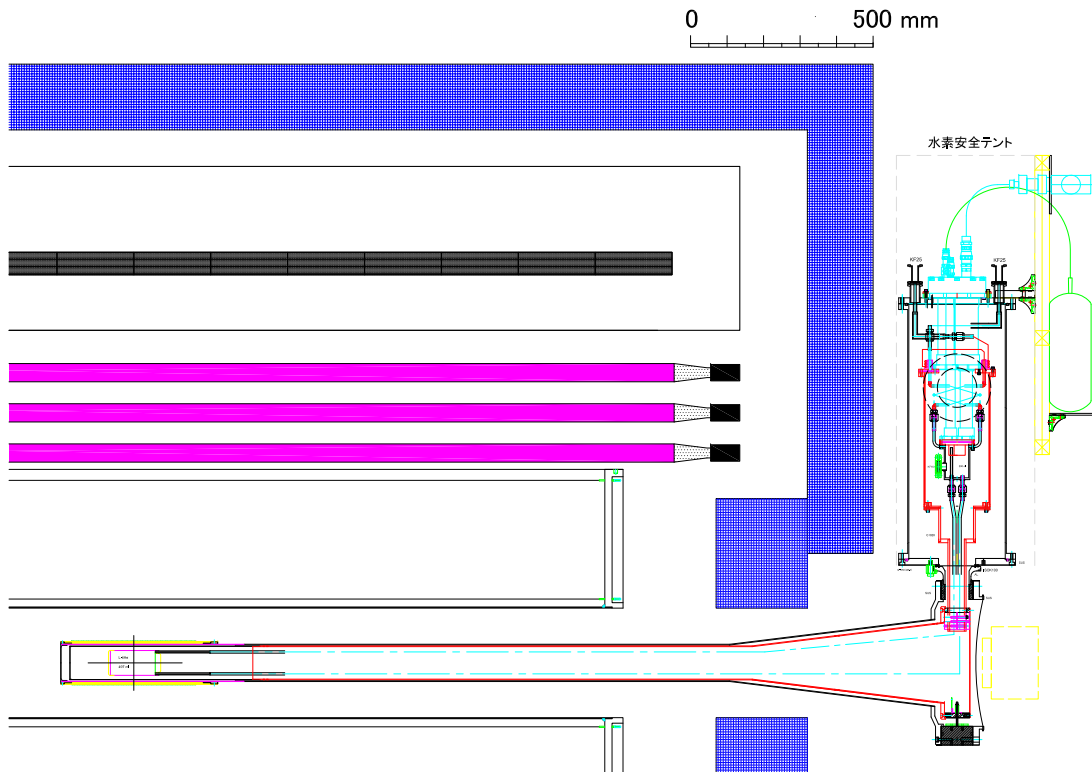


Figure 11: Schematic design of the target system with the E80 setup.

6 Cylindrical Detector System (CDS)

Efficient and high precision reconstruction of decay particles from the target region with large acceptance is a key for the E80 experiment. To this end, we newly construct a large size CDS at the K1.8BR beam line. The requirements for the CDS are as follows:

Large acceptance

The exclusive measurement of the (K^-, N) reaction is essential for the experiment. To detect particles involved in the reaction as much as possible, the detector acceptance needs to be as large as possible, for both charged and neutral particles coming from the target region. The large acceptance system can reduce backgrounds attributed to particle misidentification from missing particles.

High resolution

The spatial and timing resolution of the detector system has to be as good as possible to precisely reconstruct the decays of the kaonic nuclei and to determine its properties. At minimum, the resolution achieved with the previously used CDS is required to efficiently reconstruct the $\Lambda \rightarrow \pi^- p$, $\Sigma^\pm \rightarrow \pi^\pm n$, and $K^0 \rightarrow \pi^+ \pi^-$ decays.

Neutron detection

High detection efficiency for neutrons is a key in the E80 experiment to precisely measure the $K^- ppn \rightarrow \Lambda pn$ decay. Detection of a neutron(s) from the production and decay is also of special importance in the series of the experimental programs. In reconstruction of the sequential decay of $\Lambda(1405) \rightarrow \pi^\pm \Sigma^\mp$ followed by $\Sigma^\pm \rightarrow \pi^\pm n$, the decay neutron has low momentum of a few 100 MeV/ c . Thus we measure the neutron with time-of-flight technique using a plastic scintillator which is the best way of the low-momentum neutron measurement.

To fulfill the requirements described above, the CDS is designed to be composed of four main subsystems: a superconducting solenoid magnet, a cylindrical drift chamber (CDC), a cylindrical neutron counter (CNC), and a vertex fiber tracker (VFT). A schematic view of the CDS is shown in Fig. 12. Momenta of the decay particles from the target are reconstructed by the VFT and CDC which operate in a magnetic field of 0.7 T provided by the solenoid magnet. The first layer of the CNC is used for charged particle identification and used as a decay particle trigger.

For charged particles, the solid-angle of the new CDS defined by the first layer of the CNC is 93%, which is significantly larger than the existing CDS of 59%. Figure 13 shows a comparison of the detector acceptance between the new CDS and the existing CDS for the $K^-^4\text{He} \rightarrow \Lambda dn$ channel, which is evaluated with a full Monte-Carlo simulation. The detector acceptance of the new CDS is drastically improved as clearly seen in the figure. The enlargement of the acceptance is quite essential for the systematic investigation of kaonic nuclei to efficiently detect particles in the final state and to specify the reaction channel in unambiguous manner.

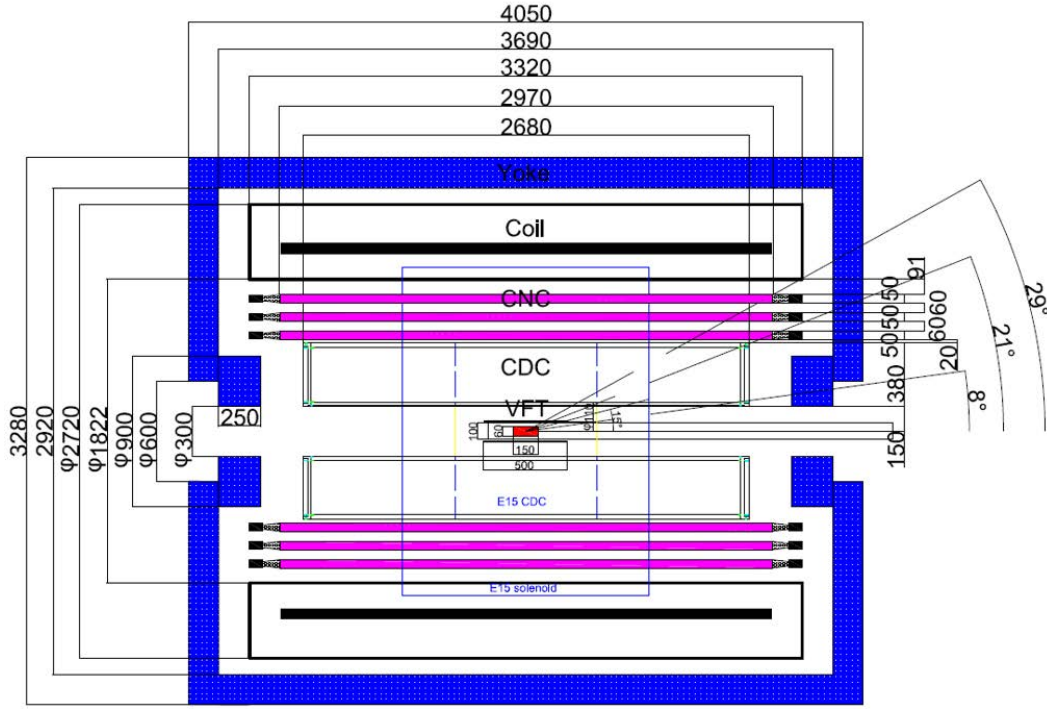


Figure 12: Design of the CDS (cross section).

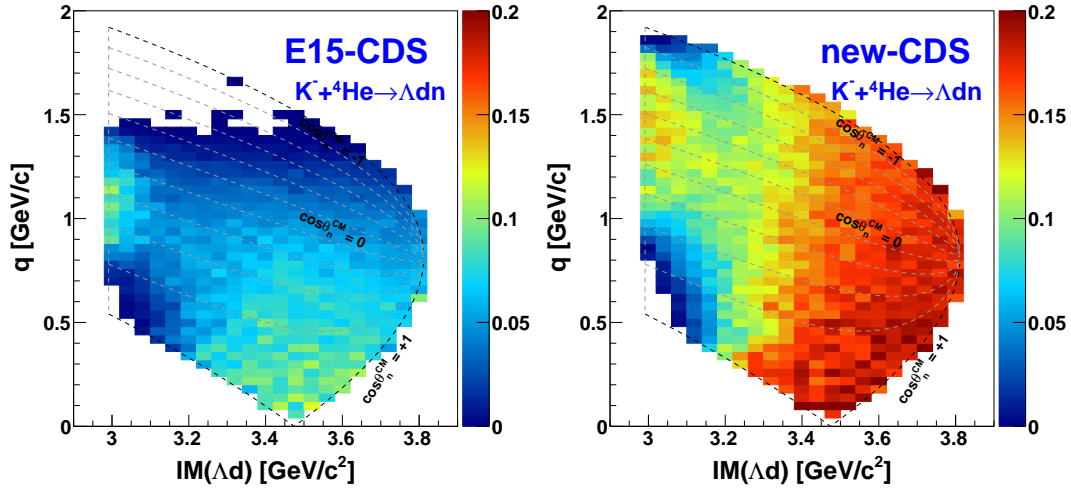


Figure 13: Detector acceptance for the Λd detection with the CDS in the $K^- + {}^4\text{He} \rightarrow \Lambda d n$ reaction. The left figure shows the acceptance with the existing CDS (E15-CDS), and the right shows that with the newly constructed CDS (new-CDS). The relation between q and $\cos(\theta_n^{CM})$ is also represented, where $\cos(\theta_n^{CM})$ denotes the polar angle of the missing neutron in the center-of-mass frame of the $K^- + {}^4\text{He}$ reactions.

Aiming at efficient neutron detection, the CNC is designed to consist of an array of scintillation counters with a total thickness of 150 mm. A typical neutron detection efficiency is $\sim 15\%$, which is five times larger than that of the existing CDS.

The component of the CDS is designed to be easily rearranged to be dedicated to individual experimental aims. For instance, to measure the spin-spin correlation of the decay Λ and proton from the $\bar{K}NN$ state for the spin/parity determination, we are planning to install a polarimeter composed of the CNC and a tracker system proposed as the P89 experiment. For precise measurement of the pure $I = 0$ $\Lambda(1405) \rightarrow \pi^0 \Sigma^0$ decay, which is the most important channel to deduce the spectral shape of the $\Lambda(1405)$, we also have a plan to install an electromagnetic calorimeter by replacing the CNC's 2nd layer and beyond in the future.

6.1 Superconducting Solenoid Magnet

A large superconducting solenoid magnet provides a strong and uniform magnetic field up to 1.0 T over the tracking volume by covering a large acceptance for outgoing particles from the target region. The magnet is under construction with the cooperation of the J-PARC cryogenics section. The design of the main components of 'the detector solenoid magnet' for the COMET Phase-I experiment is adopted for the magnet in consideration of the experimental requirements and feasibility of construction.

The parameters of the magnet are summarized in Table 3. A component called cold mass, which combines the mechanical support and cooling structure of coils wound with the NbTi/Cu superconductors, is conduction-cooled from the second stage of the Gifford-McMahon (GM) refrigerators driven by air-cooled compressors. The thermal radiation shield surrounding the cold mass is also conduction-cooled in the first stage of the GM refrigerators. The magnet has sufficient cooling capacity for the design heat load (cold mass: 4.2 W, radiation shield: 165 W) by equipping three GM refrigerators. The magnet is operated with a 2 kVA power supply (maximum output: 200A - ± 10 V). The design peak magnetic field on the conductor reaches to 1.2 T at an operation current of 189 A corresponding to the central magnetic field of 1.0 T. The magnet has a sufficient margin in superconducting properties for load line ratios below 0.3. In the E80 experiment, we will operate the magnet with the central field of 0.7 T to be able to detect low-momentum charged particles, *i.e.*, down to ~ 50 MeV/ c in the case of pions. The bore diameter of the vacuum vessel is 1.8 m and length is 3.3 m with an overall weight of 10.6 tons. The shape of the return yoke is square shape whose external dimensions is 3.3 m \times 3.3 m \times 4.1 m with an overall weight of ~ 115 tons; the magnets weigh a total of ~ 125 tons.

Table 3: Parameters of the superconducting solenoid magnet.

	Items	Unit	Value
Magnet	Center magnetic field	T	1
	Current	A	189
	Inductance	H	236
	Stored energy	MJ	4.19
	Rise time	h	2
	Cooling method		Small refrigeration machine direct cooling
	Coil protection method		Semi-active quench-back (Self-protection by diode)
Coil	Inner diameter	mm	2140
	Coil length	mm	171.7
	Coil thickness	mm	8
	Number of coils	pieces	14
	Total coil length	m	2.92
	Current density	A/mm ²	131
	Number of turns per coil	turn	945
	Total number of turns	turn	13230
Superconducting wire	Conductor dimension	mm	1.2
	Copper ratio	Cu/NbTi	4.2
	Length per coil	km	7
	Total length	km	98
Vacuum vessel	Inner diameter	mm	1800
	Outer diameter	mm	2720
	Length	mm	3320
	Barrel thickness	mm	20
	End-plate thickness	mm	50
	Weight	t	5.9
Cold mass	4K weight	t	3.6
Return yoke	Inside dimension	mm	2920
	Outside dimension	mm	3280
	Length	mm	4050
	Weight	t	~ 115
Refrigerator	Refrigeration type		Gifford-McMahon (GM) RDE-418D4 (SHI)
	Compressor type		Air-Cooled FA-50 (SHI)
	Number of Refrigerators	unit	3
	Capacity (4.2K)	W	5.4 (=1.8×3)
	Capacity (60K)	W	180 (=60×3)
Heat load	4K section	W	4.2
	Radiation shield section	W	165
Excitation power supply	AC input		AC200V – 3-phase 50Hz
	Maximum output current	A	200
	Maximum output voltage	V	±10
	Cooling method		air cooling
	Quench detector	unit	2
	Meter relay	unit	2
	Interlock system		abnormal temperature

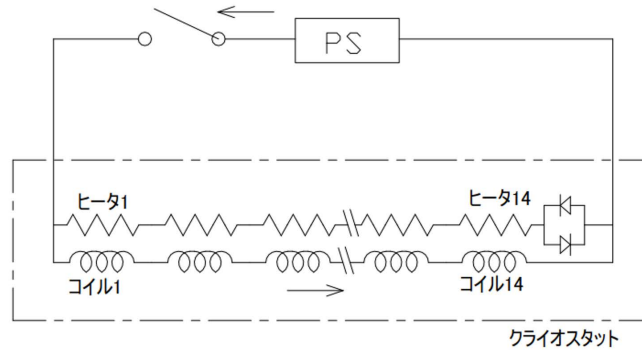


Figure 14: Quench protection circuit. (provided with the cooperation of the J-PARC Cryogenics Section)

Superconducting coil

The cold mass consists of a stack of 14 solenoid coils with the same specifications based on NbTi/Cu wire with diameter of 1.2 mm. The number of turns for each coil is 935 with a cross-sectional configuration of $171.7 \times 8 \text{ mm}^2$. The length of the superconducting wire for each coil is 7 km. The total number of the turns and the wire length are then 13,230 and 98 km, respectively. In addition, the heater by copper wire with diameter of 1.5 mm for quench protection is formed by a non-inductive winding method on each solenoid coil.

Quench protection

For the quench protection, semi-active quench-back system similar to the MuSIC superconducting solenoid magnet system at the Research Center for Nuclear Physics (RCNP) at Osaka University in Japan [41] is adopted to reduce high coil voltage over 1 kV. Figure 14 shows the quench protection circuit. All the coils are connected in series to the power supply. Voltage taps are attached to the ends of solenoid coil and the splices of the current leads for quench detection and investigation. The series-connected copper quench-back heater path is connected in parallel to the solenoid coil path via diodes. If the quench is detected, the power supply is immediately shutdown and the current in the coils is bypassed into the heater path. Then, almost all the energy stored in the magnet is dumped in the cold mass.

Figures 15 and 16 show the calculated values of current, coil temperature, heater temperature, coil voltage, and heater voltage during the quench. Current decays from 189 to 0 A in approximately 10 seconds, including quench detection time and quench-back response time. The maximum heater voltage at both ends of the heater equivalent to all coil voltages is 450 V and the maximum quench spot temperature which is the highest temperature in the coils is 150°C . These results suggest that the magnet is safely and reversibly protected.

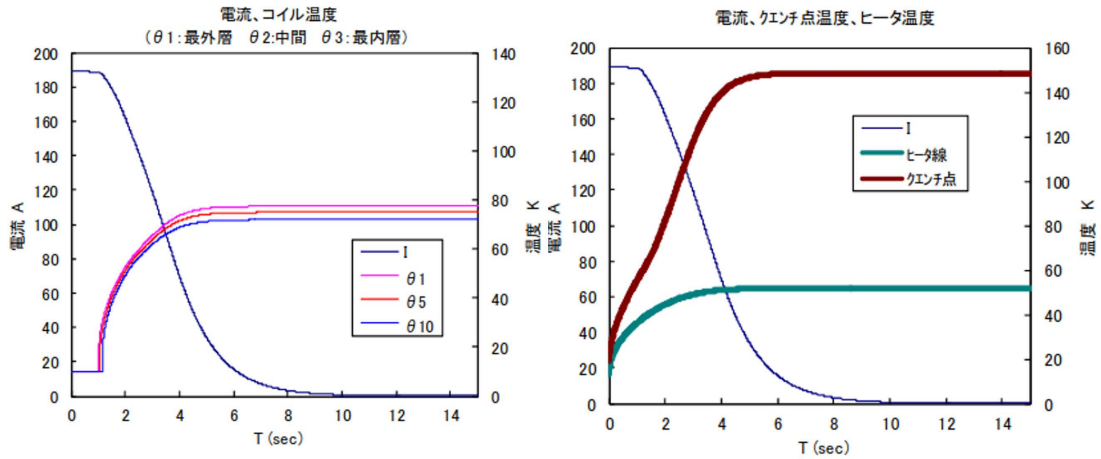


Figure 15: Time variation of current, coil temperature, and heater temperature during quench. (provided with the cooperation of the J-PARC Cryogenics Section)

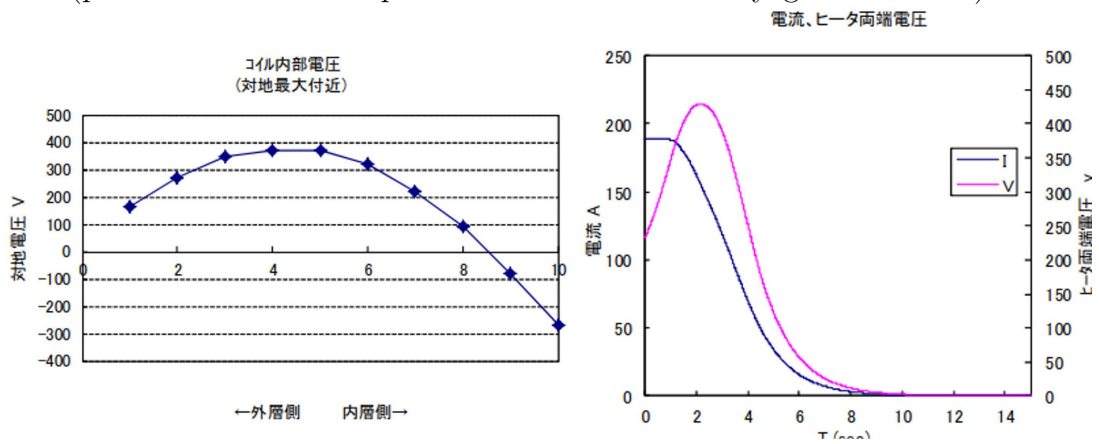


Figure 16: Coil voltage at quench, and time variation of current and voltage at both ends of heater during quench. (provided with the cooperation of the J-PARC Cryogenics Section)



Figure 17: Schematic view of the vacuum vessel. Rails, reinforcements, etc. on the inner wall are not shown. (provided with the cooperation of the J-PARC Cryogenics Section)

Vacuum vessel

Figure 17 shows a schematic view of the vacuum vessel. To allow the detector to be installed in the magnet bore, a support structure based on a rail structure will be attached. This support structure will be designed to have a load capacity of 3 tons. Preliminary structural calculations using the finite element method shows a maximum displacement of about 0.15 mm under the loaded rail.

Return yoke

The return yoke is composed of a square-shaped side-wall and end-caps as shown in Fig. 18. Each side of the side-wall is divided into three parts, 12 pieces in total, to be easily hoisted by an overhead crane with a rated load of 40 tons at the Hadron Hall. The end-cap is divided into two parts, upper and lower, and is opened and closed by the crane. To make the magnetic field in the tracking region uniform, ring-shaped yokes are installed inside the both end-caps. A refrigerator port is provided in the center of the side wall for installation of the GM refrigerators. The vacuum vessel, ports, cold head, etc. are designed so that they do not extend beyond the return yoke. The detector readout cables are taken out through holes on the four corners of the end-caps.

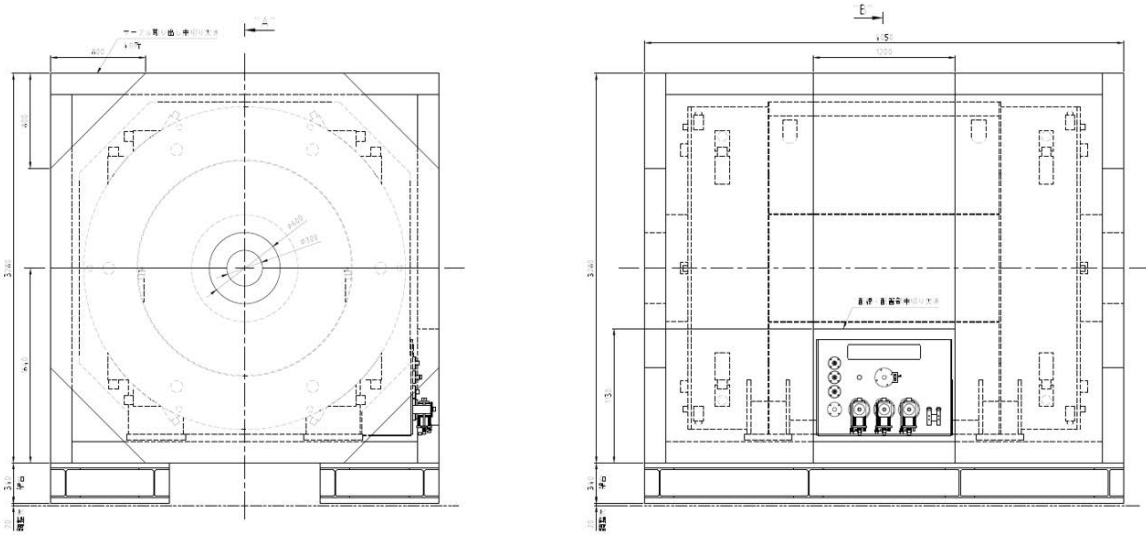


Figure 18: Schematic view of the return yoke.

Magnetic field calculation

The magnetic field distribution is calculated with a full-size 3D magnet model using OPERA simulation software package as shown in Fig. 19, where the beam direction defines the direction of the z axis in the right-handed coordinate and the y axis is directed to the upward direction. The maximum field was set to 1.0 T for all magnetic field calculations. The magnetic field distribution for the z -component (beam direction), B_z , is shown in Fig.20. In the tracking region ($r \lesssim 500$ mm), the magnetic field uniformity near the central region ($|z| \lesssim 800$ mm) is a few percent, but at the edges ($800 \lesssim |z| \lesssim 1300$ mm) it is about 10 percent. Figure21 shows the magnetic field distribution around the GM refrigerator cold-head motors ($x \sim 1518$ mm, $y \sim -1190$ mm). The magnetic field at the center of the motors is less than 20 mT, which is below the operational limit (50 mT).

Charged-particle tracking will be performed using the Runge-Kutta method or the Kalman filter based on the calculated magnetic fields. For the purpose of verifying the magnetic field calculation, magnetic field measurement will be made after the completion of the magnet. We plan to perform the field measurement using a 3D Hall probe; a magnetic field scan will be performed with respect to the z -direction (beam-axis direction) at several positions in the (x,y) plane and compared with the calculated values. Small holes will be provided in the end-caps to pass the Hall probe from the outside.

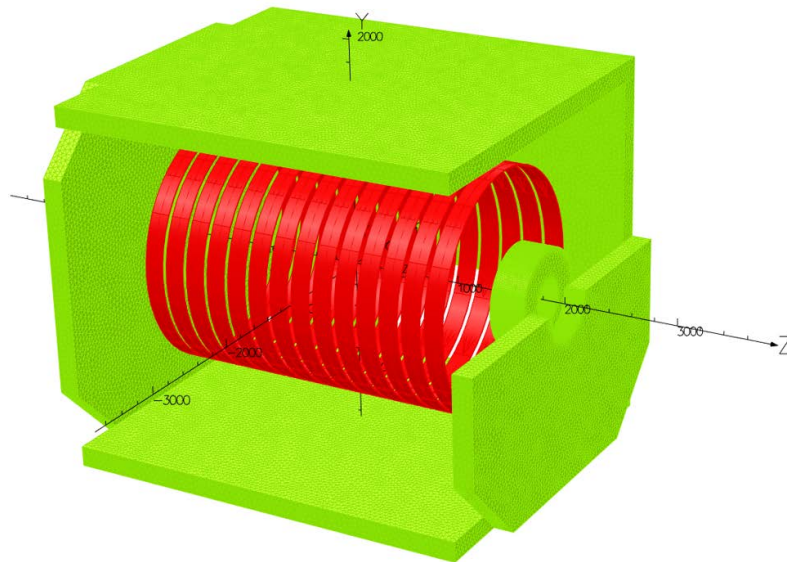


Figure 19: Magnetic field calculation model. A part of the return yoke is shown. The beam direction defines the direction of the z axis in the right-handed coordinate and the y axis is directed to the upward direction.

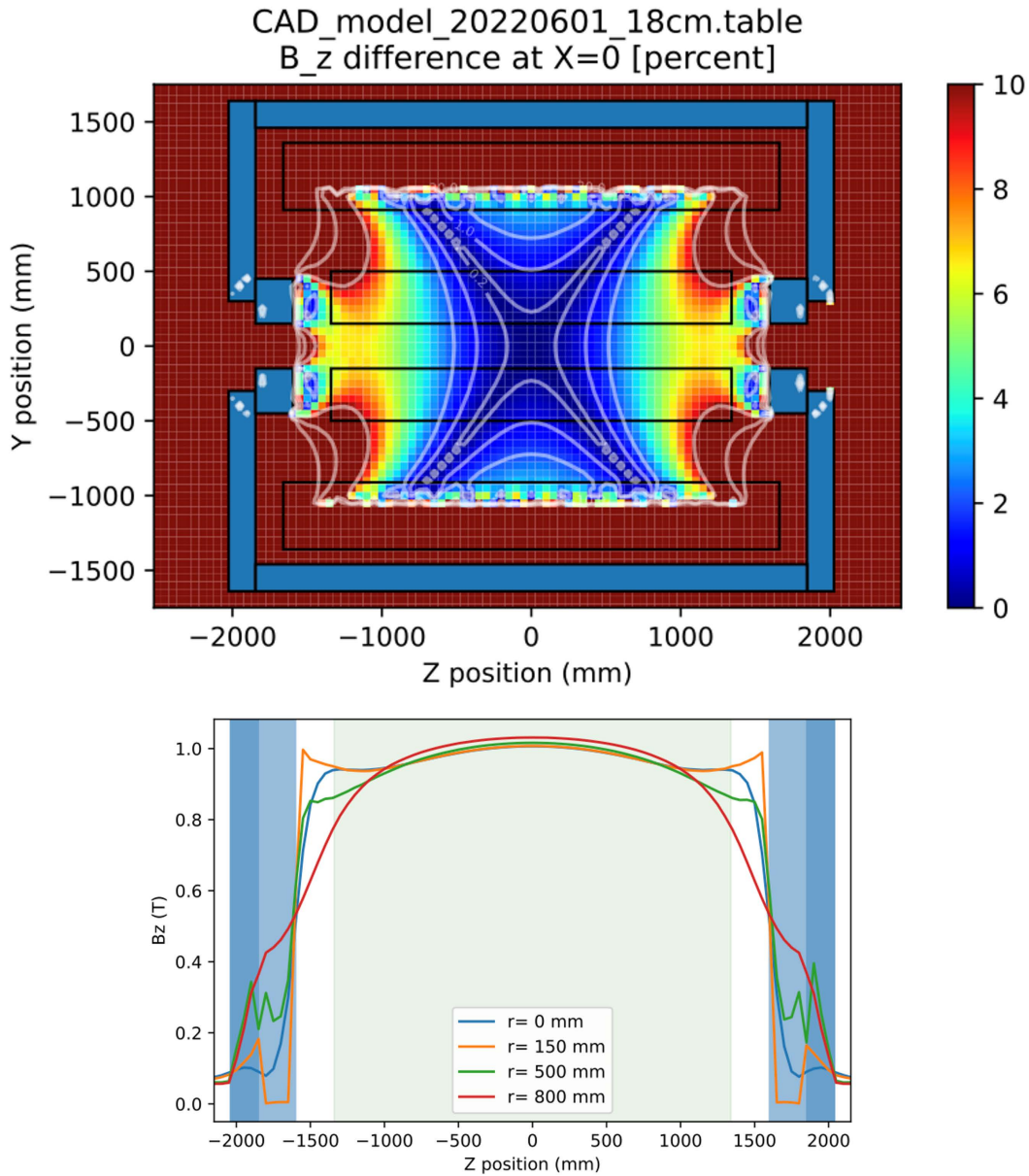


Figure 20: Calculated magnetic field distribution. (left) The z-component of the magnetic field, B_z , in the yz plane on the central beam axis. The deviation from the central magnetic field is shown as a percentage. (right) The position dependence of B_z as a function of the z axis: $r = 150, 500$ mm respectively correspond to the position of the inner and outer wall of the CDC, and $r = 800$ mm corresponds to 100 mm inside the vacuum vessel.

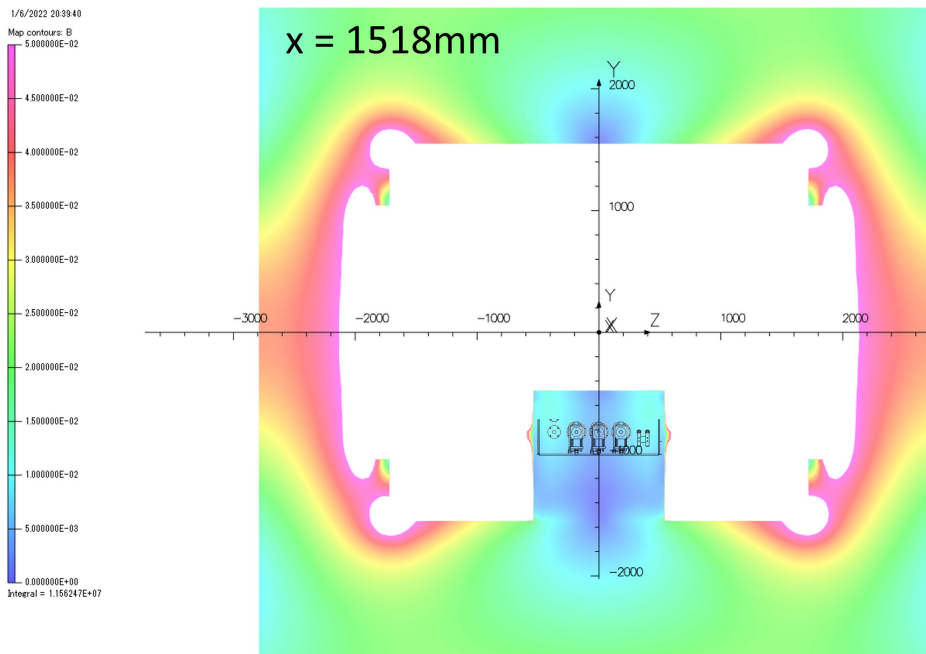
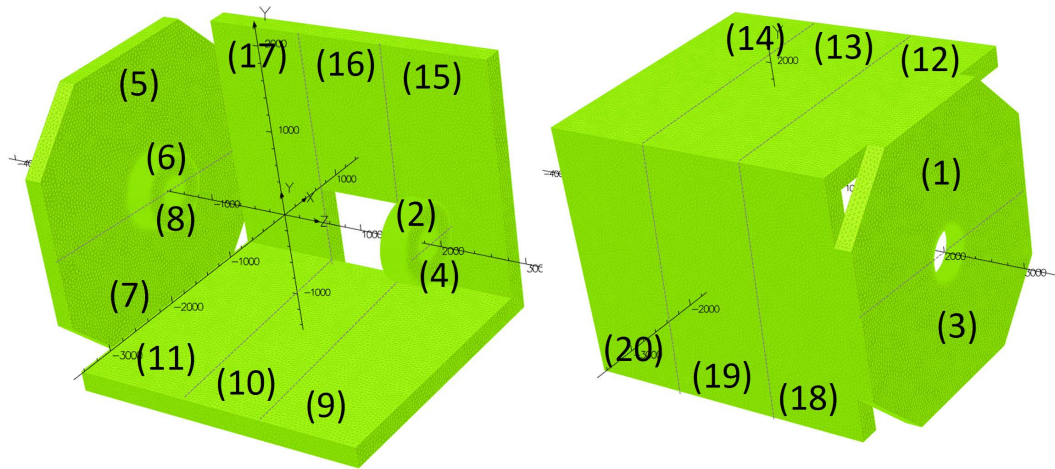


Figure 21: Calculated magnetic field distribution around the GM refrigerator cold-head motors ($x \sim 1518$ mm, $y \sim -1190$ mm). In the (z, y) plane cross section at $x = 1518$ mm, below 50 mT is shown in the color map. The magnetic field at the center of the motors is less than 20 mT, which is below the operational limit of 50 mT.

Structural calculation

We have performed structural calculations of forces on magnets. Figure 22 shows calculated electromagnetic force applied to each part of the return yoke using OPERA simulation software package. For the side-walls, the electromagnetic force that pulls them inward is about 40 tons maximum per side. For the upstream and downstream end-caps, the force that pulls the end-caps inward is about 100 tons. Figure 23 shows the calculated stresses and displacements for the end-cap using Autodesk Inventor 3D-CAD application. The analysis was performed by applying a force of 500 kN per the upper and lower end-cap to a single point near the center, which is an extreme assumption for safety. In the configuration shown in the figure, the maximum stress on a bolt is about 300 MPa which can be covered by using such as SCM435 M36 bolts. Displacement is about 1 mm near the center. The design is thus sufficiently strong to withstand the load of this electromagnetic force.



component name	Fx [N]	Fy [N]	Fz [N]
(1) cap down bottom	2	25,452	-759,143
(2) donut down bottom	107	19	206,973
(3) cap down up	29	-25,644	-776,760
(4) donut down up	107	19	206,973
(5) cap up bottom	22	25,536	757,753
(6) donut up bottom	131	-356	-206,821
(7) cap up up	116	-25,293	777,720
(8) donut up up	131	-356	-206,821

component name	Fx [N]	Fy [N]	Fz [N]
all coils (Lorentz force)	-390	226	-103

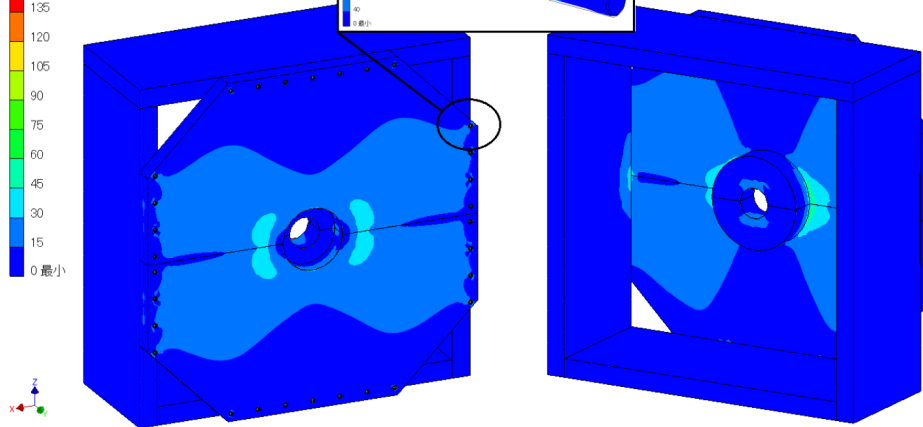
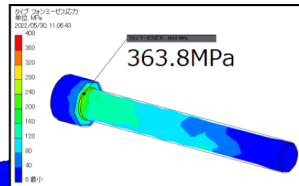
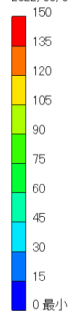
component name	Fx [N]	Fy [N]	Fz [N]
(9) bottom down	-36	22,811	-153,692
(10) bottom middle	160	622	-250
(11) bottom up	-28	22,564	153,750
(12) top down	6	-13,595	-110,830
(13) top middle	17	-876	-17
(14) top up	4	-13,672	110,961

component name	Fx [N]	Fy [N]	Fz [N]
(15) left down	-7,508	-9,926	-64,584
(16) left middle	-525	39	-166
(17) left up	-7,512	-9,660	63,407
(18) right down	7,603	692	-79,596
(19) right middle	619	22	13
(20) right up	7,602	730	79,782

Figure 22: Calculated electromagnetic force applied to each part of the return yoke using OPERA simulation software package.

応力分布

タイプ フォンミーゼス応力
単位 MPa
2022/05/30, 10:58:38



変位

タイプ 変位
単位 mm
2022/05/30, 10:58:36

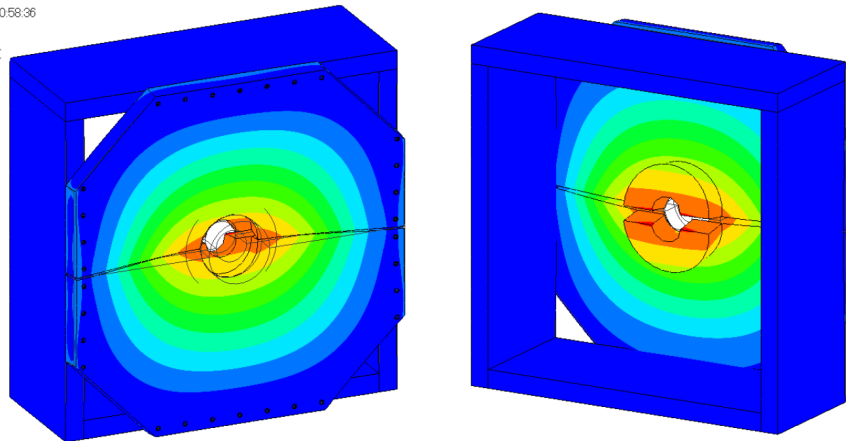
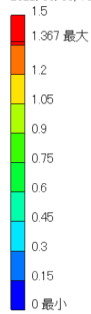


Figure 23: Calculated stresses and displacements for the end-cap using Autodesk Inventor 3D-CAD application.

Construction schedule

The construction schedule of the magnet is shown in Fig. 24. The magnet construction is a three-year project. In FY2022, we will procure superconducting wire at first, and construct the return yoke. The GM refrigerators used for conduction cooling and a power supply system with DAQ module will also be procured in this year. In FY2023-24, we will construct the magnet: cold-mass production, its assembly, cooling tests, excitation tests without the return yoke at a manufacturer. On-site assembly with the return yoke is scheduled for the end of FY2024. At the beginning of FY2025, we will perform an excitation test and magnetic field measurement under actual experimental conditions.

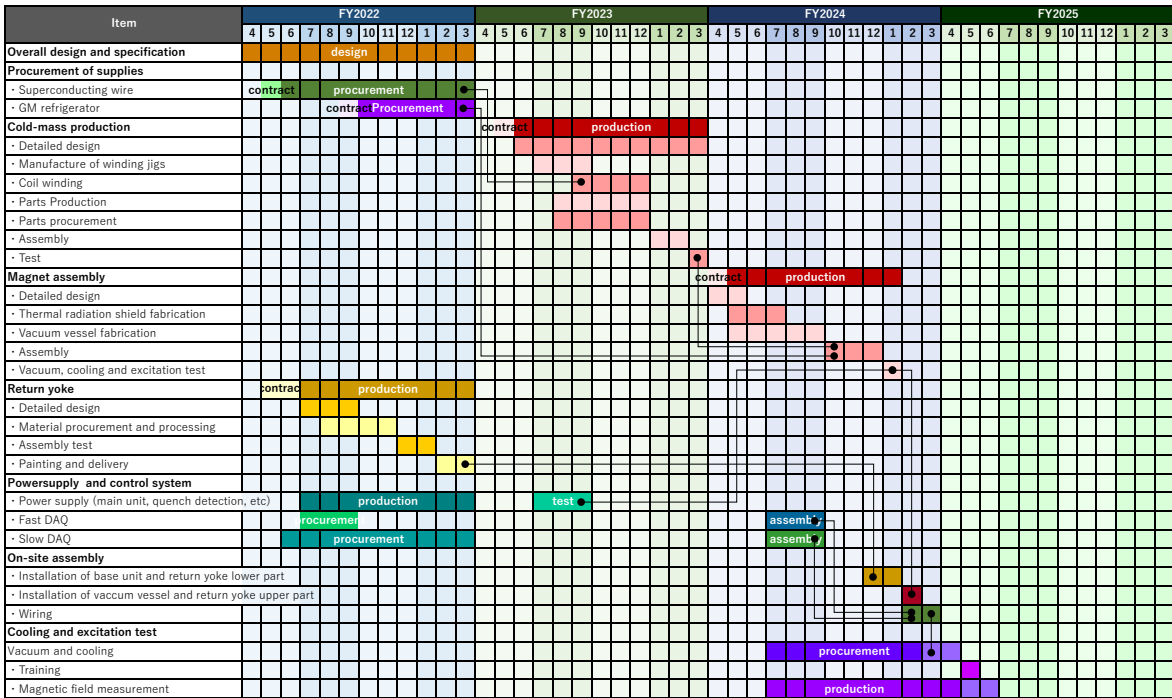


Figure 24: Construction schedule of the magnet. (provided with the cooperation of the J-PARC Cryogenics Section)

6.2 Cylindrical Drift Chamber (CDC)

The CDC is a cylindrical wire drift chamber that contains 15 layers of anode wires. The structure of the CDC is shown in Fig. 25. The outer radius is 530 mm and the inner radius is 150 mm, with a total length of 2680 mm. The wire length of axial layers is 2550 mm, thus the angular coverage is $21^\circ < \theta < 159^\circ$ in the polar angle region corresponding to a solid angle coverage of 93% of 4π .

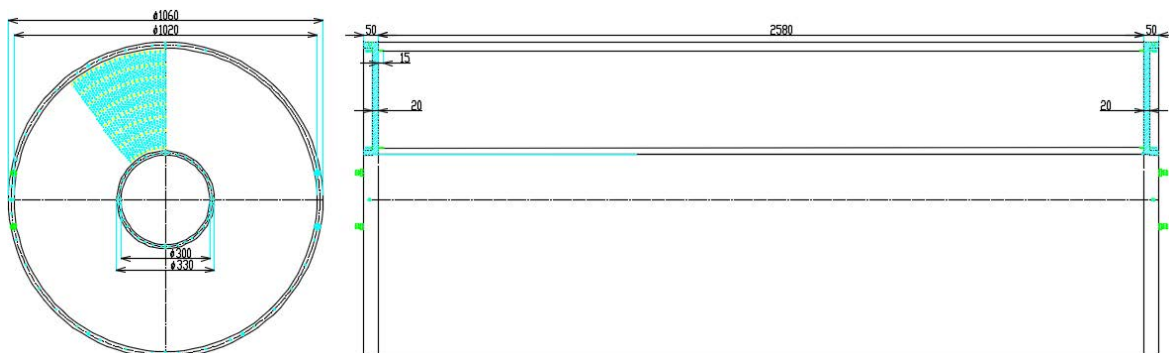


Figure 25: Design of the CDC (all dimensions in mm). The CDC consists of two aluminum end-plates, a 3 mm thick aluminum cylinder as an outer wall.

The CDC consists of two aluminum end-plates of 20 mm thickness supported by six aluminum pipes of $\phi 10$ mm. To obtain a good tracking efficiency and momentum resolution for low- p_t tracks, the CDC is designed to have a 0.3 mm mylar window as the inner wall around the target region. Thus, the CDC has a 3 mm thick aluminum cylinder with $\sim 1/3$ of the center section in mylar and a 2 mm thick aluminum cylinder as the inner and outer walls, respectively, to keep gas volume.

The same cell structure as the existing CDC is applied to the new CDC to reuse the existing signal and high-voltage circuit boards placed directly on the end-plates (Fig. 26). The CDC has 15 layers of small hexagonal cells with a typical drift length of 9 mm, which are grouped into 7 super-layers as shown in Fig. 27. Table 4 gives the detailed parameters of the wire configuration. The layers are in the radial region from 190.5 mm (layer #1) to 484.5 mm (layer #15). The 8 stereo layers tilted by about 2.7° are used to obtain longitudinal position information. The number of readout channels is 1,816 and the total number of wires in the CDC is 8,064.

The CDC uses gold-plated tungsten (Au-W) of $30 \mu\text{m}$ ϕ for the sense wires, and beryllium-copper (Be-Cu) of $80 \mu\text{m}$ ϕ for the field and guard wires. These wires are supported by feedthroughs with a bushing inserted at the end. Bushes with an 80 and 200 μm ϕ hole are used for the sense and field/guard wires, respectively. To keep the wire sag below 200 μm , tension is applied on the Au-W and Be-Cu wires by 50 g and 240 g, respectively. Table 5 summarizes the wire parameters. We have performed structural calculation with these wire tensions as shown in Fig. 28, in which we have

found that the end-plates are warped by 1.8 mm near the center at maximum. To prevent the distortion of the end-plates, pre-tension will be applied to the end-plates when wiring.

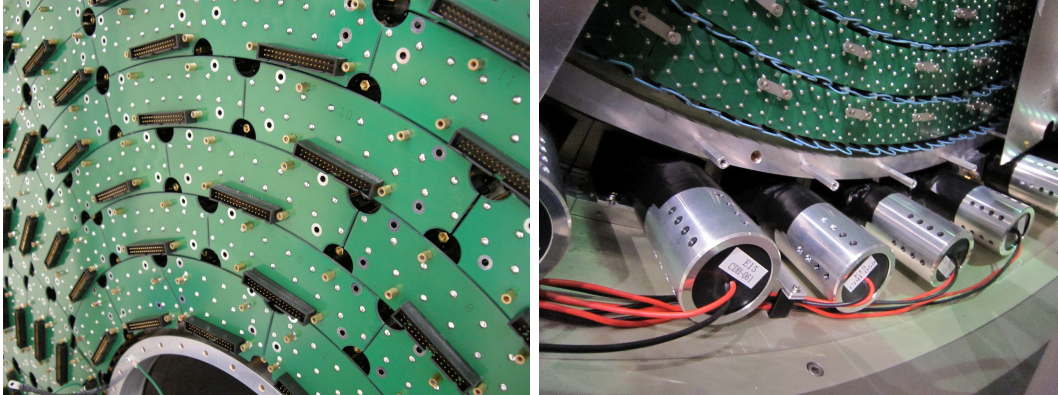


Figure 26: Existing (left) signal and (right) HV circuit boards placed directly on the end-plates of the CDC. We reuse the boards for the newly constructed CDC.

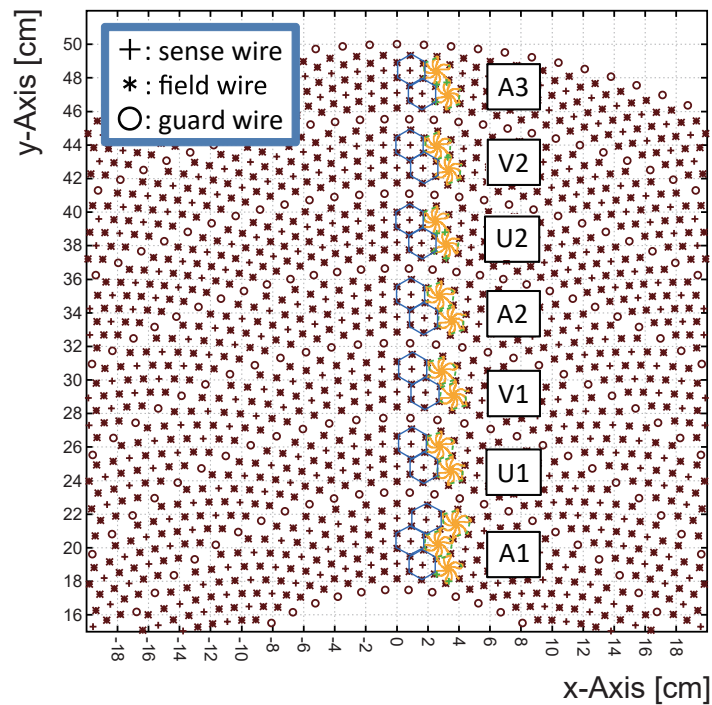


Figure 27: Cell structure of the CDC.

Table 4: Wire configuration of the CDC.

Super-layer	layer	Wire direction	Radius (mm)	Cell width (degree)	Cell width (mm)	Stereo angle (degree)	Signal channels per layer
A1	1	X	190.5		16.7	0	
	2	X'	204.0	5.00	17.8	0	72
	3	X	217.5		19.0	0	
U1	4	U	248.5	4.00	17.3	-2.27	90
	5	U'	262.0		18.3	-2.39	
V1	6	V	293.0	3.60	18.4	2.42	100
	7	V'	306.5		19.3	2.53	
A2	8	X	337.5	3.00	17.7	0	120
	9	X'	351.0		18.4	0	
U2	10	U	382.0	2.40	16.0	-2.82	150
	11	U'	395.5		16.6	-2.92	
V2	12	V	426.5	2.25	16.7	2.96	160
	13	V'	440.0		17.3	3.05	
A3	14	X	471.0	2.00	16.4	0	180
	15	X'	484.5		16.9	0	

Table 5: Wire parameter of the CDC.

Wire type	Wire diameter	Wire material	Number of wires	Wire tension
sense	$\phi 30 \mu\text{m}$	Au-W	1,816	50 g
filed	$\phi 80 \mu\text{m}$	Be-Cu	5,376	240 g
guard	$\phi 80 \mu\text{m}$	Be-Cu	1,052	240 g

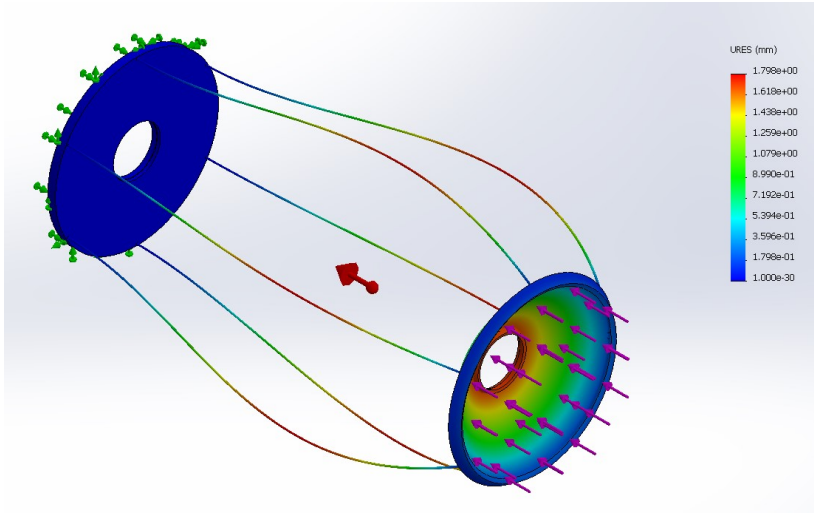


Figure 28: Structural calculation of the CDC.

The drift gas is mixed argon (50%)-ethane (50%) at 1 atm. A high voltage is applied to the field and guard wires, and the sense wires are kept at ground potential. For the first super-layer (A1) and the second one (U1), a high voltage of -2.8 kV will be applied to the potential wires, and -2.7 kV to the potential wires of the other super-layers. In addition, -1.5 kV, -1.8 kV, and -0.6 kV will be applied to the innermost, the outermost, and the other guard wires, respectively. Using these applied voltages, the layer efficiencies of the CDC are expected to be over 99%, which have been achieved with the existing CDC. A typical intrinsic resolution of 200 μm is expected, which corresponds to the transverse-momentum (p_t) resolution of $5.3\% p_t \oplus 0.5\%/\beta$ (σ). The readout electronics of the CDC consists of a preamp card with ASDs (SONY-CXA3653Q, $\tau = 16$ ns) and HUL multi-hit TDCs, which has been used for the existing CDC.

The construction of the CDC will be completed in FY2023; feedthroughs and other necessary materials will be procured in FY2022, and the assembly and wiring will be done in FY2023.

6.3 Cylindrical Neutron Counter (CNC)

The CNC is an array of segmented plastic scintillation counters used for the neutron detection. The first layer of the NC is also used for the charged-particle identification as a hodoscope counter. The CNC has a thickness of 15 cm divided into three layers. The first layer of the CNC is located at a radius of 550 mm from the beam axis covering a polar angle range from 21 to 159 degrees corresponding to a solid angle coverage of 93% of 4π which is designed to be the same as the CDC. The second and third layers are located at 660 mm and 770 mm, respectively. A solid angle coverage of the CNC is $29^\circ < \theta < 151^\circ$ in the polar angle region corresponding to a solid angle

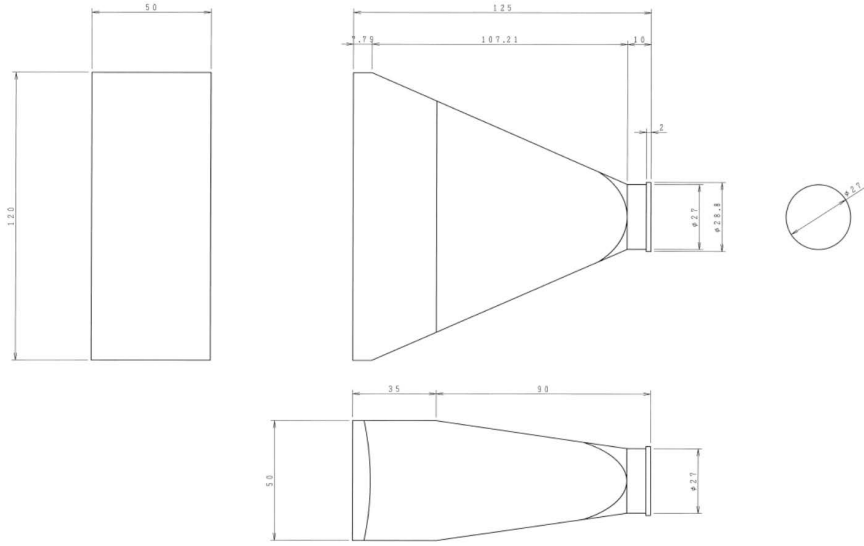


Figure 29: (top) A prototype module of the CNC. (bottom) A prototype design of the CNC light guide.

coverage of 87% of 4π . The expected neutron detection efficiency is 15% ~ 45% which depends on the neutron momentum.

The CNC consists of 32 modules in a layer whose scintillators are made of Eljen EJ-200 with dimensions of 50 mm in thickness, 2.97 m in length, and ~ 113 mm (layer 1) / 135 mm (layer 2) / 156 mm (layer 3) in width. The scintillation light is transferred through light guides to a pair of Hamamatsu R7761 fine-mesh 19-dynode photomultipliers (FM-PMT) 1.5 inches in diameter (H8409). These photomultipliers are the same type as those used in the Cylindrical Detector Hodoscope (CDH, with Eljen EJ-200 scintillators of 790 mm in length, 99 mm in width, and 30 mm in thickness) at the existing solenoid spectrometer. Thus we will reuse the photomultipliers that we have about 100, and the design of the light guide will be similar to that of the existing CDH.

The CNC will be operated in the 0.7 T magnetic field with a typical PMT gain

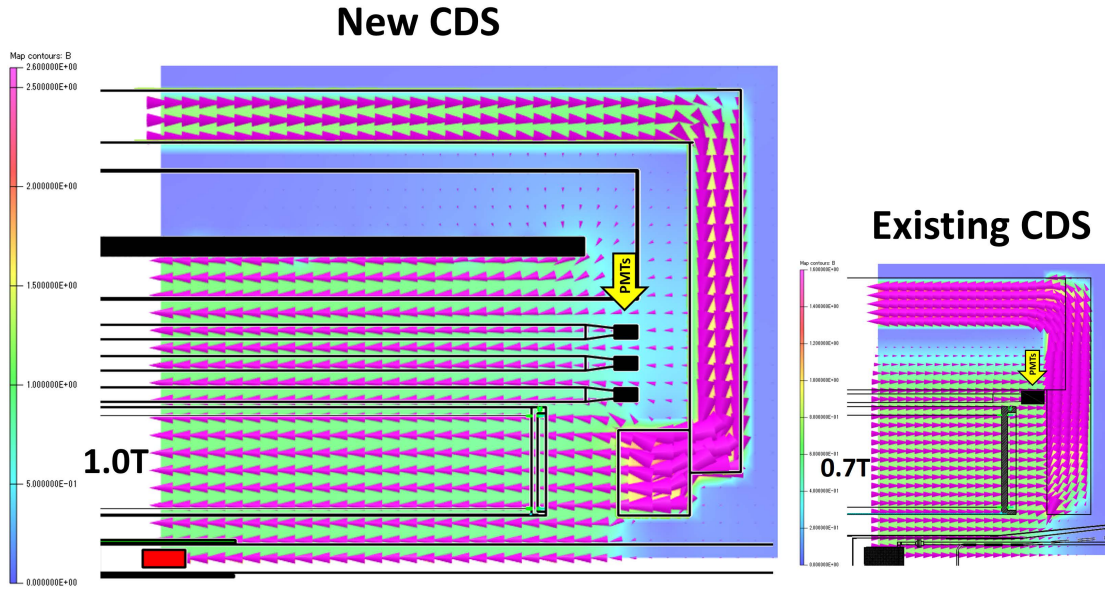


Figure 30: Magnitude and direction of the calculated magnetic field of (left) the new CDS and (right) the existing CDS.

of $\sim 10^6$, as in the case of the existing CDH. Figure 30 shows a comparison of the magnitude and direction of the calculated magnetic field between the new CDS and the existing CDS. The magnetic-field direction at the location of the FM-PMT is approximately parallel to the photomultiplier axis in both cases. At the existing CDS, the FM-PMT gain of approximately 10^6 has been safely achieved under 0.7 T operation, thus the FM-PMT will also work fine in the new CDS. The expected average time resolution of the CNC without a magnetic field is ~ 70 ps (σ), whose details are now examined using a prototype module shown in Fig. 29.

The first layer of the CNC will be delivered in FY2022, and its assembly will take place in FY2023 followed by a performance test with cosmic rays. We will use the same readout system currently used for the CDH, *i.e.*, CAEN V792 QDC and HUL HR-TDC.

6.4 Vertex Fiber Tracker (VFT)

The high-resolution vertex determination is indispensable to discriminate between the signals and backgrounds with event topology such as distance of closest approach method. With only the CDC, the vertex resolution of the beam direction (z-direction) is expected to be ~ 1 cm, while that of the radius direction (r-direction) is a few mm. This is due to small tilt angles of the stereo layers which is limited by the wire layout. By introducing the VFT, the vertex resolution in the beam direction will be improved to a few mm with a combination of the CDC tracking information. The momentum

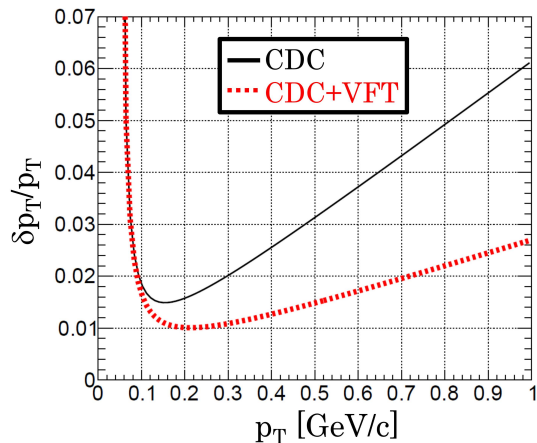


Figure 31: Comparison of the transverse momentum resolution (σ) between the CDC alone and the CDC+VFT.

resolution is also expected to be improved by introducing the VFT as shown in Fig. 31.

The VFT is installed on the outer wall of the target chamber ($r \sim 55$ mm) covering a polar angle range from 15 to 165 degrees corresponding to a solid angle coverage of 97% of 4π . We use 4 layers of 1 mm ϕ scintillating fibers having $UU'VV'$ configuration. In the U and V layers, the fibers are tilted by ± 45 degrees. The total readout channel is 896 ($= 224 \times 4$). For readout, VME EASIROC modules developed by the Open-It group or a system developed for the fiber-tracker system in the E50 experiment will be used.

The VFT will be installed to the existing CDS in FY2022 aiming to use it as the vertex tracker for the E73 experiment, the direct measurement of hypertriton lifetime. We will use the same system for the E80 setup as it is.

6.5 Support Structure of the CDS

For safe installation and easy maintenance of the detector, the design of a support structure of the internal detector of the CDS is of importance. In particular, it is crucial how well the structurally weak detector is supported and accurately placed in position. Due to spatial limitations upstream of the K1.8BR area, the detector should be installed from downstream of the beam.

To achieve these goals, a structure supporting the CNC will be built stand-alone or built into the end-cap of the CDC, and the CDC and CNC will be assembled as one unit outside the magnet at the beam height (2 m). A conceptual design of the support structure for the CDC and CNC is shown in Fig. 32. Then, the detector unit will be installed by sliding it on inner-wall rails of the vacuum vessel. As the rail for the support structure, Linear Motion Guide (LM-guide) will be mounted on the inner

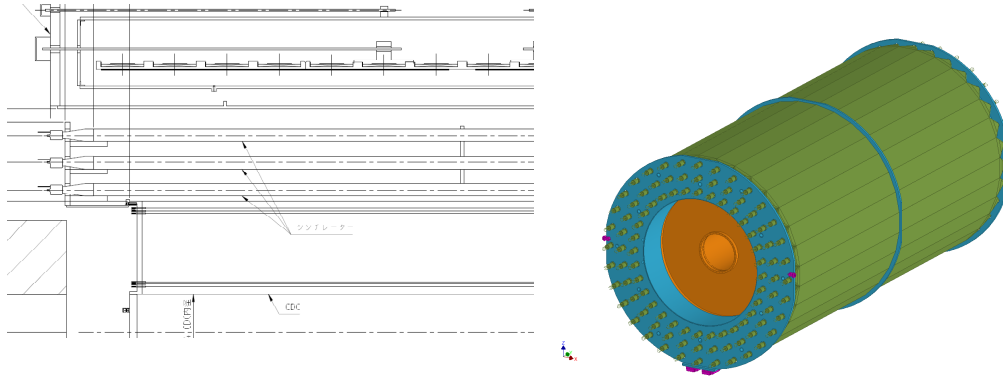


Figure 32: Conceptual design of a support structure for the CDC and CNC: (left) schematic drawing of how the CDC and CNC are combined and (right) 3D model of an assembled unit.

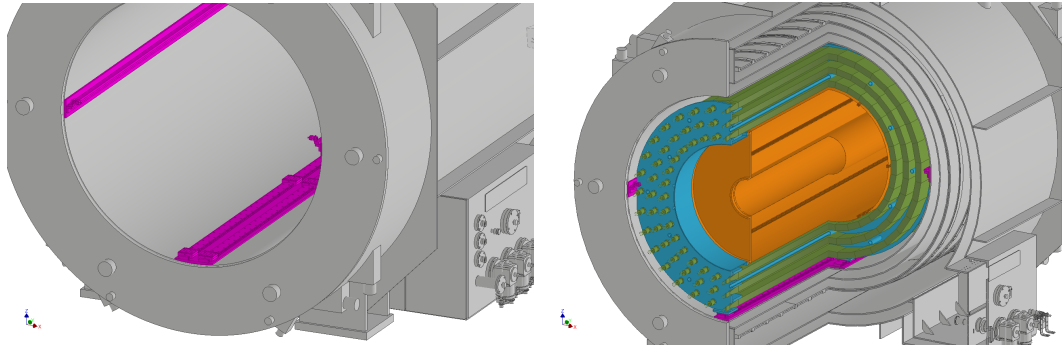


Figure 33: (left) Conceptual design of a rail system built on the inner wall of the vacuum vessel. (right) CDS assembled with a conceptual design of the support structure and the rail system.

wall of the vacuum vessel. Since the total weight of the CDC and CNC including the support structure will be approximately 2.5 tons, the rail system will be designed to withstand a load of 3 tons. Figure 33(left) shows a conceptual design of the rail system, in which two LM-guides are installed in parallel at the bottom of the inner wall with additional guide rails in the horizontal position to prevent run out during insertion. The CDS assembled with this conceptual design is shown in Fig. 33(right).

To construct the detector unit and to smoothly connect it to the inner-wall rails, a similar rail structure will be built outside of the magnet, *i.e.*, right next to the magnet entrance. When the detector maintenance is needed, the whole detector unit can be uninstalled from inside the magnet using the rail system.

7 Trigger and DAQ systems

A dedicated hardware trigger will be developed to meet experimental requirements. The kaon beam trigger is constructed with the same procedure as the previously performed experiments at the K1.8BR beam line. The elementary beam trigger is constructed by coincidence signals from the beam line counters (BHT*T0), and the kaon beam trigger is selected from the beam trigger by using the kaon identification counter (\overline{AC}).

To select an event associated with the K^-ppn decay, we will use the simplest charged-multiplicity trigger implemented at the hardware level with the first layer of the CNC (fCNC). For the measurement of $K^-^4\text{He} \rightarrow "K^-ppn" n \rightarrow \Lambda dn \rightarrow \pi^- pdn$, three hits of the fCNC (fCNC_3) is used; three charged particles ($\pi^- pd$) are required in the CDS to reconstruct the " K^-ppn " $\rightarrow \Lambda d$ decay. This trigger also covers detection of the $K^-^4\text{He} \rightarrow "K^-ppn" n \rightarrow \Lambda pnn \rightarrow \pi^- ppnn$ event.

We use the HDDAQ framework as the online data acquisition system, whose maximum accumulation rate has been confirmed to reach to ~ 10 k events per spill with more than 90% DAQ efficiency. In the E80 experiment, the expected trigger rate of the main trigger, fCHC_3, is ~ 4 kHz by taking into account the result of the previous experiments as summarized in Table 6. Therefore, the trigger rate is controllable.

Table 6: Measured and estimated trigger rate. The trigger rate of E80 with the CDS (Kaon*fCNC_n) is estimated using the T77 results by taking into account the increased beam power and solid angle: estimated trigger rate = T77 (51kW/5.2s \sim 63kW/4.2s) $\times 90/63 \times 1.4 \times 93\%/59\% = \text{T77} * 3.2$.

	51kW (T77, Run85)	90kW (E80)
Beam (BHD[BHT]*T0)	940k	1,900k
Pion_all (Beam*AC)	430k	860k
Kaon_all (Beam* \overline{AC})	260k	520k
Kaon (Beam* \overline{AC} *DEF)	210k	420k
Kaon*CDH_1[fCNC_1]	13k	41k
Kaon*CDH_2[fCNC_2]	4k	12k
Kaon*CDH_3[fCNC_3]	1.3k	4.0k

8 Acknowledgments

We gratefully acknowledge all the staff members at KEK/J-PARC/JAEA. In particular, we would like to sincerely thank the members of the J-PARC Cryogenics Section and the hadron beam line group for the great deal of support made to design and construct the superconducting solenoid magnet.

References

- [1] M. Iwasaki *et al.* *Phys. Rev. Lett.* **78** (1997) 3067.
- [2] G. Beer *et al.* *Phys. Rev. Lett.* **94** (2005) 212302.
- [3] M. Bazzi *et al.* *Phys. Lett.* **B704** (2011) 113.
- [4] A. D. Martin *Nucl. Phys.* **B179** (1981) 33.
- [5] Y. Nogami *Phys. Lett.* **7** (1963) 288.
- [6] Y. Akaishi and T. Yamazaki *Phys. Rev.* **C65** (2002) 044005.
- [7] T. Yamazaki and Y. Akaishi *Phys. Lett.* **B535** (2002) 70.
- [8] N. V. Shevchenko, A. Gal, and J. Mares *Phys. Rev. Lett.* **98** (2007) 082301.
- [9] N. V. Shevchenko, A. Gal, J. Mares, and J. Révai *Phys. Rev.* **C76** (2007) 044004.
- [10] Y. Ikeda and T. Sato *Phys. Rev.* **C76** (2007) 035203.
- [11] A. Doté, T. Hyodo, and W. Weise *Nucl. Phys.* **A804** (2008) 197.
- [12] Y. Ikeda and T. Sato *Phys. Rev.* **C79** (2009) 035201.
- [13] S. Wycech and A. M. Green *Phys. Rev.* **C79** (2009) 014001.
- [14] A. Doté, T. Hyodo, and W. Weise *Phys. Rev.* **C79** (2009) 014003.
- [15] Y. Ikeda, H. Kamano, and T. Sato *Prog. Theor. Phys.* **124** (2010) 533–539.
- [16] N. Barnea, A. Gal, and E. Z. Liverts *Phys. Lett.* **B712** (2012) 132.
- [17] M. Bayar and E. Oset *Phys. Rev.* **C88** (2013) 044003.
- [18] S. Maeda, Y. Akaishi, and T. Yamazaki *Proc. Jpn. Acad.* **B89** (2013) 418.
- [19] J. Révai and N. V. Shevchenko *Phys. Rev.* **C90** (2014) 034004.
- [20] A. Doté, T. Inoue, and T. Myo *Prog. Theor. Exp. Phys.* **2015** (2015) 043D02.

- [21] T. Sekihara, E. Oset, and A. Ramos *Prog. Theor. Exp. Phys.* **2016** (2016) 123D03.
- [22] S. Ohnishi, W. Horiuchi, T. Hoshino, K. Miyahara, and T. Hyodo *Phys. Rev.* **C95** (2017) 065202.
- [23] A. Doté, T. Inoue, and T. Myo *Phys. Rev.* **C95** (2017) 062201.
- [24] A. Doté, T. Inoue, and T. Myo *Phys. Lett.* **B784** (2018) 405.
- [25] M. Agnello *et al.* *Phys. Rev. Lett.* **94** (2005) 212303.
- [26] T. Yamazaki *et al.* *Phys. Rev. Lett.* **104** (2010) 132502.
- [27] Y. Ichikawa *et al.* *Prog. Theor. Exp. Phys.* **2015** no. 2, (2015) 021D01.
- [28] O. Vázquez Doce *et al.* *Phys. Lett.* **B758** (2016) 134.
- [29] R. Del Grande *et al.* *Eur. Phys. J.* **C79** (2019) 190.
- [30] G. Agakishiev *et al.* *Phys. Lett.* **B742** (2015) 242.
- [31] A. O. Tokiyasu *et al.* *Phys. Lett.* **B728** (2014) 616.
- [32] T. Hashimoto *et al.* *Prog. Theor. Exp. Phys.* **2015** (2015) 061D01.
- [33] Y. Sada *et al.* *Prog. Theor. Exp. Phys.* **2016** (2016) 051D01.
- [34] S. Ajimura *et al.* *Phys. Lett.* **B789** (2019) 620.
- [35] T. Yamaga *et al.* *Phys. Rev. C* **102** (2020) 044002.
- [36] Letter of Intent for J-PARC, 2009, "Double Anti-kaon Production in Nuclei by Stopped Anti-proton Annihilation"
http://j-parc.jp/researcher/Hadron/en/Proposal_e.html .
- [37] T. Kishimoto *Phys. Rev. Lett.* **83** (1999) 4701.
- [38] Proposal for J-PARC, 2021, "Proposal for the E80 Phase-I Experiment: Investigation of the $\bar{K}NNN$ Bound State Focusing on the Λd Decay"
http://j-parc.jp/researcher/Hadron/en/Proposal_e.html .
- [39] J. Allison *et al.* *Nucl. Instrum. Meth.* **A835** (2016) 186.
- [40] O. Sasaki and M. Yoshida *IEEE Transactions on Nuclear Science* **46** (1999) 1871.
- [41] M. Yoshida *et al.* *IEEE Transactions on Applied Superconductivity* **21** (2011) 1752.